

# Cosmological Constraints from a Combination of Galaxy Clustering & Lensing – I. Theoretical Framework

Frank C. van den Bosch<sup>1\*</sup>, Surhud More<sup>2</sup>, Marcello Cacciato<sup>3</sup>, Houjun Mo<sup>4</sup>, Xiaohu Yang<sup>5</sup>

<sup>1</sup>*Department of Astronomy, Yale University, PO. Box 208101, New Haven, CT 06520-8101*

<sup>2</sup>*Kavli Institute for Cosmological Physics, University of Chicago, 933 East 56<sup>th</sup> Street, Chicago, IL 60637*

<sup>3</sup>*Racah Institute of Physics, The Hebrew University, Jerusalem 91904, Israel*

<sup>4</sup>*Department of Astronomy, University of Massachusetts, Amherst MA 01003-9305*

<sup>5</sup>*Key Laboratory for Research in Galaxies and Cosmology, Shanghai Astronomical Observatory, Nandan Road 80, Shanghai 200030, China*

## ABSTRACT

We present a new method that simultaneously solves for cosmology and galaxy bias on non-linear scales. The method uses the halo model to analytically describe the (non-linear) matter distribution, and the conditional luminosity function (CLF) to specify the halo occupation statistics. For a given choice of cosmological parameters, this model can be used to predict the galaxy luminosity function, as well as the two-point correlation functions of galaxies, and the galaxy-galaxy lensing signal, both as function of scale and luminosity. These observables have been reliably measured from the Sloan Digital Sky Survey. In this paper, the first in a series, we present the detailed, analytical model, which we test against mock galaxy redshift surveys constructed from high-resolution numerical  $N$ -body simulations. We demonstrate that our model, which includes scale-dependence of the halo bias and a proper treatment of halo exclusion, reproduces the 3-dimensional galaxy-galaxy correlation and the galaxy-matter cross-correlation (which can be projected to predict the observables) with an accuracy better than 10 (in most cases 5) percent. Ignoring either of these effects, as is often done, results in systematic errors that easily exceed 40 percent on scales of  $\sim 1h^{-1}$  Mpc, where the data is typically most accurate. Finally, since the projected correlation functions of galaxies are never obtained by integrating the redshift space correlation function along the line-of-sight out to infinity, simply because the data only cover a finite volume, they are still affected by residual redshift space distortions (RRSDs). Ignoring these, as done in numerous studies in the past, results in systematic errors that easily exceed 20 percent on large scales ( $r_p \gtrsim 10h^{-1}$  Mpc). We show that it is fairly straightforward to correct for these RRSDs, to an accuracy better than  $\sim 2$  percent, using a mildly modified version of the linear Kaiser formalism.

**Key words:** galaxies: halos — large-scale structure of Universe — dark matter — cosmological parameters — gravitational lensing — methods: statistical

## 1 INTRODUCTION

The past decade has seen the emergence of precision cosmology. Various experiments that probe fluctuations in the cosmic microwave background (CMB), most notably the Wilkinson Microwave Anisotropy Probe (WMAP; Bennett et al. 2003) have yielded constraints on various cosmological parameters at the few percent level (Spergel et al. 2003,

2007; Dunkley et al. 2009; Komatsu et al. 2009, 2011), and ongoing experiments, such as PLANCK, will tighten these constraints even further. It is important, though, to complement these data with non-CMB constraints, such as those provided by supernova Ia, galaxy clustering, galaxy peculiar velocities, cluster abundances, gravitational lensing, Lyman  $\alpha$  forest and, in the not too distant future, 21cm tomography of the neutral hydrogen at the era of reionization. These non-CMB constraints are crucial for (i) breaking var-

\* E-mail: frank.vandenbosch@yale.edu

ious parameter degeneracies inherent in the CMB data <sup>†</sup>, (ii) constraining certain cosmological parameters that are largely unconstrained by the CMB, such as evolution in the equation of state of dark energy, and (iii) for establishing a true concordance cosmology, i.e., a cosmological model that is in agreement with all possible data sets.

With the advent of ever larger and more homogeneous galaxy redshift surveys, such as the Las Campanas Redshift Survey (LCRS; Shectman et al. 1996), the PSCz (Saunders et al. 2000), the two-Degree Field Galaxy Redshift Survey (2dFGRS; Colless et al. 2003) and the Sloan Digital Sky Survey (SDSS; York et al. 2000), there has been a steady improvement in the tightness and reliability of the corresponding cosmological constraints. Most of these studies focus on using galaxy clustering on large scales where one can rely on linear theory. Prime examples are constraints from (baryon acoustic oscillations in) the galaxy power spectrum (Percival et al. 2001; Cole et al. 2005; Eisenstein et al. 2005; Tegmark et al. 2006; Hütsi 2006; Percival et al. 2007a,b,c; Padmanabhan et al. 2007; Gaztanaga, Cabré & Hui 2009; Percival et al. 2010; Blake et al. 2011; Anderson et al. 2012).

However, recently it has also become feasible to accurately model galaxy clustering on small, non-linear scales using the halo model approach combined with halo occupation statistics. The halo model postulates that all dark matter is partitioned over dark matter haloes, and describes the dark matter density distribution in terms of the halo building blocks (e.g., Neyman & Scott 1952; Seljak 2000; Ma & Fry 2000; Scoccimarro et al. 2001; Cooray & Sheth 2002). When combined with a model that describes how galaxies with certain properties are distributed over dark matter haloes of different mass, this can be used to make predictions for the clustering properties of galaxies on all scales that are observationally accessible (e.g., Jing, Mo & Börner 1998; Berlind & Weinberg 2002; Cooray & Sheth 2002; Yang, Mo & van den Bosch 2003).

This approach has been used extensively in recent years to constrain the galaxy-dark matter connection, i.e., the connection between galaxy properties and halo mass, which holds important information regarding galaxy formation. On large, linear scales, the two-point correlation function between haloes of mass  $M$  can be written as  $\xi_{\text{hh}}(r|M) = b_{\text{h}}^2(M) \xi_{\text{mm}}^{\text{lin}}(r)$ , with  $\xi_{\text{mm}}^{\text{lin}}(r)$  the two-point correlation function of the linear matter distribution and  $b_{\text{h}}(M)$  the linear halo bias (e.g., Mo & White 1996). Similarly, for galaxies of a given luminosity, one has that  $\xi_{\text{gg}}(r|L) = b_{\text{g}}^2(L) \xi_{\text{mm}}^{\text{lin}}(r)$ , with  $b_{\text{g}}(L)$  the bias of galaxies of luminosity  $L$ . Hence, one can use  $\xi_{\text{gg}}(r|L)$  to infer the *average* mass of haloes that host galaxies of luminosity  $L$  by simply finding the  $M$  for which  $b_{\text{h}}(M) = [\xi_{\text{gg}}(r|L)/\xi_{\text{mm}}^{\text{lin}}(r)]^{1/2}$ . By comparing the observed abundance of galaxies of luminosity  $L$  to the predicted abundance of haloes of mass  $M$ , one subsequently infers the average number of galaxies per halo. Hence, measurements of  $\xi_{\text{gg}}(r|L)$  can be used to constrain halo occupation statistics, and this technique has been widely used (Jing et al. 1998, 2002; Peacock & Smith 2000; Bullock, Wechsler & Somerville 2002; Magliocchetti & Porciani 2003;

Yang et al. 2003, 2004; van den Bosch et al. 2003a, 2007; Porciani, Magliocchetti & Norberg 2004; Wang et al. 2004; Zehavi et al. 2004, 2005; Zheng 2004; Abazajian et al. 2005; Collister & Lahav 2005; Tinker et al. 2005, 2006; Lee et al. 2006). Note, though, that this method requires knowledge of both  $b_{\text{h}}(M)$  and  $\xi_{\text{mm}}^{\text{lin}}(r)$ , both of which are strongly cosmology dependent. Consequently, the resulting halo occupation statistics are also cosmology dependent (see e.g., Zheng et al. 2002; Berlind & Weinberg 2002; van den Bosch et al. 2007; Cacciato et al. 2009). Although this makes it difficult to calibrate galaxy formation models using halo occupation statistics (e.g., Berlind et al. 2003), it also implies that one can use this method to constrain cosmological parameters as long as one has some independent constraints on halo occupation statistics.

Various approaches to constrain cosmological parameters along these lines have been used in recent years. Abazajian et al. (2005) have shown that the degeneracy between occupation statistics and cosmology can (at least partially) be broken by using the correlation function itself, as long as one includes data on sufficiently small scales (i.e., the one-halo term). Using the projected correlation functions measured from the SDSS and allowing the cosmological parameters to vary within constraints imposed by various CMB experiments, they were able to obtain constraints that were significantly tighter than those from the CMB alone, with  $\Omega_{\text{m}} = 0.26 \pm 0.03$  and  $\sigma_8 = 0.83 \pm 0.04$ .

Zheng et al. (2002) suggested that one can break the degeneracy between halo occupation model and cosmology by using the peculiar velocities of galaxies as inferred from the redshift space distortions in the two-point correlation function. This idea was used by Yang et al. (2004), who concluded that the power-spectrum normalization,  $\sigma_8$ , needs to be of the order of  $\sim 0.75$  (assuming  $\Omega_{\text{m}} = 0.3$ ), significantly lower than the value then advocated by WMAP. Very similar results were obtained by van den Bosch et al. (2007) and by Tinker et al. (2007). The latter used a much more sophisticated treatment of redshift space distortions developed by Tinker, Weinberg & Zheng (2006) and Tinker (2007).

An alternative approach for breaking the degeneracy between halo occupation model and cosmology is to use constraints on the (average) mass-to-light ratios of dark matter haloes. This method was first used by van den Bosch et al. (2003b) and Tinker et al. (2005), who were able to obtain relatively tight constraints on  $\Omega_{\text{m}}$  and  $\sigma_8$  from combinations of clustering data plus constraints on the mass-to-light ratios of clusters. Interestingly, both studies again found evidence for a relatively low value of the power spectrum normalization:  $\sigma_8 \simeq 0.75$  for  $\Omega_{\text{m}} = 0.25$ .

Along similar lines, one can also use a combination of clustering and galaxy-galaxy lensing. The latter effectively probes the galaxy-dark matter cross correlation, and therefore holds information regarding the mass-to-light ratios of dark matter haloes covering a wide range in halo mass. Since its first detection by Brainerd, Blandford & Smail (1996), the accuracy of galaxy-galaxy lensing measurements has increased to the extent of yielding high signal-to-noise ratio measurements over a significant dynamic range in galaxy luminosity and/or stellar mass (e.g., Fisher et al. 2000; Hoekstra et al. 2002; Sheldon et al. 2004, 2009; Mandelbaum et al. 2006, 2009; Leauthaud et al. 2007). Similar to the galaxy-galaxy autocorrelation function, the galaxy-matter

<sup>†</sup> for instance, the CMB as measured by WMAP is consistent with a closed Universe with Hubble parameter  $h = 0.3$  and no cosmological constant (e.g. Spergel et al. 2007)

cross correlation function can be accurately modeled using the halo model (Guzik & Seljak 2001, 2002; Mandelbaum et al. 2005; Yoo et al. 2006; Cacciato et al. 2009; Leauthaud et al. 2011, 2012; van Uitert et al. 2011). Hence, the combination of galaxy clustering and galaxy-galaxy lensing is ideally suited to constrain cosmological parameters, as demonstrated in detail by Yoo et al. (2006). A first application of this idea by Seljak et al. (2005), using the model of Guzik & Seljak (2002) and the galaxy-galaxy lensing data of Mandelbaum et al. (2006), combined with WMAP constraints, yielded  $\sigma_8 = 0.88 \pm 0.06$ , only marginally consistent with the values obtained from the cluster mass-to-light ratios and/or the redshift space distortions mentioned above. However, more recently, two different analyses based on the same galaxy-galaxy lensing data by Cacciato et al. (2009) and Li et al. (2009) both argued that a flat  $\Lambda$ CDM cosmology with  $(\Omega_m, \sigma_8) = (0.238, 0.734)$  is in much better agreement with the data than a  $(0.3, 0.9)$  model. Although the reason for the disagreement between these studies and that of Seljak et al. (2005) is probably related to the different modelling approaches, these studies all have demonstrated that a combination of clustering and lensing data holds great potential for constraining cosmological parameters.

This is the first paper in a series in which we use a combination of galaxy clustering and galaxy-galaxy lensing data to constrain cosmological parameters. In this paper we present the theoretical framework and test the accuracy of our method using mock data. In More et al. 2012a (hereafter Paper II) we present a Fisher matrix analysis to identify parameter-degeneracies and to assess the accuracy with which various cosmological parameters can be constrained using the methodology presented here. Finally, in Cacciato et al. 2012b (hereafter Paper III) we apply our analysis to the actual SDSS data to constrain cosmological parameters (in particular  $\Omega_m$  and  $\sigma_8$ ) under the assumption of a ‘standard’ flat  $\Lambda$ CDM cosmology.

Throughout this paper, unless specifically stated otherwise, all radii and densities will be in comoving units, and log is used to refer to the 10-based logarithm. Quantities that depend on the Hubble parameter will be written in units of  $h = H_0/(100 \text{ km s}^{-1} \text{ Mpc}^{-1})$ .

## 2 MODEL DESCRIPTION

Our main goal is to use galaxy clustering and galaxy-galaxy lensing, measured as function of luminosity from the main galaxy sample in the SDSS, to simultaneously constrain cosmology and halo occupation statistics. As detailed in papers II and III, the data that we will use consists of (i) the galaxy luminosity function,  $\Phi(L, z)$ , at the median redshift of the SDSS main galaxy sample ( $z \simeq 0.1$ ), (ii) the projected two-point correlation functions,  $w_p(r_p|L_1, L_2, z)$ , for galaxies in six luminosity bins,  $[L_1, L_2]$ , each with its own median redshift  $z$ , and (iii) the corresponding excess surface densities (ESD),  $\Delta\Sigma(R|L_1, L_2, z)$ .

The projected correlation function,  $w_p(r_p|L_1, L_2, z)$ , is related to the corresponding galaxy-galaxy correlation function in real space,  $\xi(r|L_1, L_2, z)$ , via a simple Abel integral

$$w_p(r_p|L_1, L_2, z) = 2 \int_{r_p}^{\infty} \xi_{\text{gg}}(r|L_1, L_2, z) \frac{r dr}{\sqrt{r^2 - r_p^2}}, \quad (1)$$

(but see §2.3 below). The ESD,  $\Delta\Sigma(R|L_1, L_2, z)$ , is related to the tangential shear,  $\gamma_t(R|L_1, L_2, z)$ , measured around galaxies (the lenses) at redshift  $z$  with luminosities in the range  $[L_1, L_2]$  according to

$$\begin{aligned} \Delta\Sigma(R|L_1, L_2, z) &= \bar{\Sigma}(< R|L_1, L_2, z) - \Sigma(R|L_1, L_2, z) \\ &= \gamma_t(R|L_1, L_2, z) \Sigma_{\text{crit}}. \end{aligned} \quad (2)$$

Here  $\Sigma_{\text{crit}}$  is a geometrical parameter that depends on the comoving distances of the sources and lenses,  $\Sigma(R|L_1, L_2, z)$  is the azimuthally-averaged projected surface mass density of the gravitational lenses, which is related to the galaxy-matter cross correlation function,  $\xi_{\text{gm}}(r|L_1, L_2, z)$ , according to

$$\begin{aligned} \Sigma(R|L_1, L_2, z) &= 2 \bar{\rho}_m(z) \\ &\int_R^{\infty} [1 + \xi_{\text{gm}}(r|L_1, L_2, z)] \frac{r dr}{\sqrt{r^2 - R^2}}, \end{aligned} \quad (3)$$

and  $\bar{\Sigma}(< R|L_1, L_2, z)$  is its average inside  $R$ ;

$$\bar{\Sigma}(< R|L_1, L_2, z) = \frac{2}{R^2} \int_0^R \Sigma(R'|L_1, L_2, z) R' dR', \quad (4)$$

(Miralda-Escudé 1991; Sheldon et al. 2004; see also §2.2).

In this section, we present analytical expressions for  $w_p(r_p|L_1, L_2, z)$ ,  $\Delta\Sigma(R|L_1, L_2, z)$  and  $\Phi(L, z)$ . For completeness and clarity we present a detailed, step-by-step derivation of our method, and we will emphasize where it differs from that of previous authors. The backbone of our model is the halo model, in which the matter distribution in the Universe is described in terms of its halo building blocks (see Cooray & Sheth 2002 and Mo, van den Bosch & White 2010 for comprehensive reviews). After a detailed description of how the halo model can be used to compute the power spectrum of the dark matter mass distribution (§2.1), we show how the halo model can be complemented with a model for halo occupation statistics which allows one to compute  $w_p(r_p|L_1, L_2, z)$ ,  $\Delta\Sigma(R|L_1, L_2, z)$  and  $\Phi(L, z)$  for a given cosmology.

In order to keep the derivations concise, in what follows we will not explicitly write down the dependencies on  $L_1$  and  $L_2$ .

### 2.1 The halo model

Throughout this paper we define dark matter haloes as spherical overdensity regions with a radius,  $r_{200}$ , inside of which the average density is 200 times the average density of the Universe. Hence, the mass of a halo is

$$M = \frac{4\pi}{3} 200 \bar{\rho}_m r_{200}^3. \quad (5)$$

Under the assumption that all dark matter is bound in virialized dark matter haloes, the density perturbation field at redshift  $z$ , defined by

$$\delta_m(\mathbf{x}, z) \equiv \frac{\rho_m(\mathbf{x}, z)}{\bar{\rho}_m} - 1, \quad (6)$$

can be written in terms of the spatial distribution of dark matter haloes and their internal density profiles. Throughout we assume that dark matter haloes are spherically symmetric and have a density profile,  $\rho_h(r|M, z) =$

$M u_h(r|M, z)$ , that depends only on mass,  $M$ , and redshift,  $z$ . Note that  $\int u_h(\mathbf{x}|M, z) d^3\mathbf{x} = 1$ .

Now imagine that space (at some redshift  $z$ ) is divided into many small volumes,  $\Delta V_i$ , which are so small that none of them contains more than one halo center. The occupation number of haloes in the  $i^{\text{th}}$  volume,  $\mathcal{N}_{h,i}$ , is therefore either 0 or 1, and so  $\mathcal{N}_{h,i} = \mathcal{N}_{h,i}^2 = \mathcal{N}_{h,i}^3 \dots$ . In terms of these occupation numbers the density field of the (dark) matter can formally be written as

$$\rho_m(\mathbf{x}, z) = \sum_i \mathcal{N}_{h,i} M_i u_h(\mathbf{x} - \mathbf{x}_i|M_i, z), \quad (7)$$

where  $M_i$  is the mass of the halo whose center is in  $\Delta V_i$ . Using that the ensemble average  $\langle \mathcal{N}_{h,i} M_i u_h(\mathbf{x} - \mathbf{x}_i|M_i, z) \rangle$  is equal to  $\int dM n(M, z) M \Delta V_i u_h(\mathbf{x} - \mathbf{x}_i|M, z)$ , where  $n(M, z)$  is the halo mass function, we have that

$$\begin{aligned} \langle \rho_m(\mathbf{x}, z) \rangle &= \int dM M n(M, z) \sum_i \Delta V_i u_h(\mathbf{x} - \mathbf{x}_i|M, z) \\ &= \int dM M n(M, z) \int d^3\mathbf{x}' u_h(\mathbf{x} - \mathbf{x}'|M, z) \\ &= \bar{\rho}_m, \end{aligned} \quad (8)$$

where the last equality follows from the normalization of  $u_h(\mathbf{x}|M, z)$  and from the halo model ansatz that all dark matter is partitioned over dark matter haloes.

Similar to  $\delta_m$  we can also define the halo density contrast  $\delta_h$ . Ignoring possible stochasticity in the relation between  $\delta_m$  and  $\delta_h$ , we can use a Taylor series expansion to write

$$\delta_h(\mathbf{x}; M, z) = \delta_h(\delta_m) = \sum_{n=0}^{\infty} \frac{b_{h,n}(M, z)}{n!} \delta_m^n(\mathbf{x}, z), \quad (9)$$

(Fry & Gaztanaga 1993; Mo, Jing & White 1997), where  $b_{h,n}$  is called the halo bias factor of order  $n$ . Although the requirement that  $\langle \delta_h \rangle = 0$  implies that  $b_{h,0} = -\sum_{n=2}^{\infty} b_{h,n} \langle \delta_m^n \rangle / n!$ , which in general is not zero, one can ignore  $b_{h,0}$  since in Fourier space it only contributes to the galaxy power spectrum for wavevector  $\mathbf{k} = 0$ . Furthermore, on large scales we have that  $|\delta_m| \ll 1$ , so that we can also neglect the higher-order ( $n > 1$ ) bias factors. Hence, on large scales the cross correlation function of haloes of mass  $M_1$  and haloes of mass  $M_2$  can be written as

$$\xi_{hh}(r|M_1, M_2, z) \simeq b_h(M_1, z) b_h(M_2, z) \xi_{mm}^{\text{lin}}(r, z), \quad (10)$$

where  $\xi_{mm}^{\text{lin}}(r, z)$  is the two-point correlation function of the initial density perturbation field, linearly extrapolated to redshift  $z$ , and we have used  $b_h(M, z)$  as shorthand notation for the linear halo bias  $b_{h,1}(M, z)$ . One can extend this prescription to the mildly non-linear regime, in which one can no longer ignore the higher-order bias terms, by replacing  $\xi_{mm}^{\text{lin}}(r, z)$  with the *non-linear* two-point matter correlation function,  $\xi_{mm}(r, z)$ , and by including a radial dependence of the halo bias,  $\zeta(r, z)$  (which effectively captures the effect of the higher-order bias parameters, see §3.4 below). Under the assumption that haloes are spherical, one then obtains that

$$1 + \xi_{hh}(r|M_1, M_2, z) = [1 + b_h(M_1, z) b_h(M_2, z) \zeta(r, z) \xi_{mm}(r, z)] \Theta(r - r_{\text{min}}), \quad (11)$$

where  $\Theta(x)$  is the Heaviside step function, which assures that  $\xi_{hh}(r, z|M_1, M_2) = -1$  for  $r < r_{\text{min}}$  in order to account for halo exclusion, i.e., the fact that dark matter haloes cannot overlap. In principle, one expects that  $r_{\text{min}} = r_{\text{min}}(M_1, M_2, z) = r_{200}(M_1, z) + r_{200}(M_2, z)$ . However, the halo finder used by Tinker et al. (2008), whose halo mass function we use, *does* allow overlap of haloes in that any halo is considered a host halo as long as its center does not lie within the outer radius of another halo. Therefore, to be consistent, we follow Tinker et al. (2012) and Leauthaud et al. (2011), and adopt that  $r_{\text{min}} = \text{MAX}[r_{200}(M_1, z), r_{200}(M_2, z)]$ .

For computational convenience, we will be working in Fourier space. To that extent we define the Fourier transform of  $\rho_m(\mathbf{x}, z)$  as

$$\begin{aligned} \tilde{\rho}_m(\mathbf{k}, z) &\equiv \frac{1}{V} \int \rho_m(\mathbf{x}, z) e^{-i\mathbf{k}\cdot\mathbf{x}} d^3\mathbf{x} \\ &= \frac{1}{V} \sum_i \mathcal{N}_{h,i} M_i \tilde{u}_h(\mathbf{k}|M_i, z) e^{-i\mathbf{k}\cdot\mathbf{x}_i}, \end{aligned} \quad (12)$$

where  $V$  is the volume over which the Universe is assumed to be periodic, and

$$\tilde{u}_h(\mathbf{k}|M, z) \equiv \int u(\mathbf{x}|M, z) e^{-i\mathbf{k}\cdot\mathbf{x}} d^3\mathbf{x}, \quad (13)$$

is the Fourier transform of the normalized halo density profile. With our definition of the Fourier transform, the (non-linear) matter-matter power spectrum is defined as

$$\begin{aligned} P_{mm}(\mathbf{k}, z) &= V \langle |\delta_m(\mathbf{k})|^2 \rangle \\ &= \frac{V}{\bar{\rho}_m^2} \langle \tilde{\rho}_m(\mathbf{k}, z) \tilde{\rho}_m^*(\mathbf{k}, z) \rangle - V \delta^{\text{D}}(\mathbf{k}), \end{aligned} \quad (14)$$

where

$$\delta^{\text{D}}(\mathbf{k}) = \frac{1}{V} \int e^{-i\mathbf{k}\cdot\mathbf{x}} d^3\mathbf{x}, \quad (15)$$

is the Dirac delta function,  $\rho^*$  indicates the complex conjugate of  $\rho$ , and we have used that  $\tilde{\rho}_m(0) = \bar{\rho}_m$ .

Using Eq. (12) we have that

$$\begin{aligned} \langle \tilde{\rho}_m(\mathbf{k}, z) \tilde{\rho}_m^*(\mathbf{k}, z) \rangle &= \frac{1}{V^2} \sum_i \sum_j \\ &\langle \mathcal{N}_{h,i} M_i \mathcal{N}_{h,j} M_j \tilde{u}_h(\mathbf{k}|M_i, z) \tilde{u}_h^*(\mathbf{k}|M_j, z) e^{-i\mathbf{k}\cdot(\mathbf{x}_i - \mathbf{x}_j)} \rangle, \end{aligned} \quad (16)$$

which we split in two terms: the one-halo term, for which  $j = i$ , and the two-halo term with  $j \neq i$ . The former can be written as

$$\begin{aligned} \langle \tilde{\rho}_m(\mathbf{k}, z) \tilde{\rho}_m^*(\mathbf{k}, z) \rangle^{\text{1h}} &= \frac{1}{V^2} \sum_i \langle \mathcal{N}_{h,i} M_i^2 |\tilde{u}_h(\mathbf{k}|M_i, z)|^2 \rangle \\ &= \frac{1}{V} \int dM M^2 n(M, z) |\tilde{u}_h(\mathbf{k}|M, z)|^2, \end{aligned} \quad (17)$$

where we have used that  $\mathcal{N}_{h,i}^2 = \mathcal{N}_{h,i}$ . For the 2-halo term we use the fact that we are free to choose  $\Delta V_i$  arbitrary small, so that

$$\begin{aligned} \langle \tilde{\rho}_m(\mathbf{k}, z) \tilde{\rho}_m^*(\mathbf{k}, z) \rangle^{\text{2h}} &= \frac{1}{V^2} \int d^3\mathbf{y}_1 \int d^3\mathbf{y}_2 \\ &\int dM_1 M_1 n(M_1, z) \tilde{u}_h(\mathbf{k}|M_1, z) \end{aligned}$$

$$\int dM_2 M_2 n(M_2, z) \tilde{u}_h^*(\mathbf{k}|M_2, z) [1 + \xi_{\text{hh}}(\mathbf{y}_1 - \mathbf{y}_2, z|M_1, M_2)] e^{-i\mathbf{k}\cdot(\mathbf{y}_1 - \mathbf{y}_2)}. \quad (18)$$

Here we have accounted for the fact that dark matter haloes are clustered, as described by the two-point halo-halo correlation function  $\xi_{\text{hh}}(\mathbf{r}, z|M_1, M_2)$ .

Hence, using Eq. (11), which properly accounts for halo exclusion, we have that

$$\langle \tilde{\rho}_m(\mathbf{k}, z) \tilde{\rho}_m^*(\mathbf{k}, z) \rangle^{2\text{h}} = \frac{1}{V} \int dM_1 M_1 n(M_1, z) \tilde{u}_h(\mathbf{k}|M_1, z) \int dM_2 M_2 n(M_2, z) \tilde{u}_h(\mathbf{k}|M_2, z) Q(k|M_1, M_2, z). \quad (19)$$

Here we have used that  $\tilde{u}_h^*(\mathbf{k}|M, z) = \tilde{u}_h(\mathbf{k}|M, z)$ , which follows from the fact that  $u(\mathbf{x}|M, z)$  is real and even, and we have defined

$$Q(k|M_1, M_2, z) \equiv 4\pi \int_{r_{\text{min}}}^{\infty} [1 + \xi_{\text{hh}}(r, z|M_1, M_2)] \frac{\sin kr}{kr} r^2 dr, \quad (20)$$

with  $k = |\mathbf{k}|$  and with  $\xi_{\text{hh}}(r, z|M_1, M_2)$  given by Eq. (11).

Combining Eqs. (14)-(19), and using that haloes are defined to be spherically symmetric, we finally obtain that

$$P_{\text{mm}}(\mathbf{k}, z) = P_{\text{mm}}^{\text{1h}}(k, z) + P_{\text{mm}}^{\text{2h}}(k, z) - V \delta^{\text{D}}(\mathbf{k}), \quad (21)$$

where

$$P_{\text{mm}}^{\text{1h}}(k, z) = \frac{1}{\bar{\rho}_m^2} \int dM M^2 n(M, z) |\tilde{u}_h(k|M, z)|^2, \quad (22)$$

and

$$P_{\text{mm}}^{\text{2h}}(k, z) = \frac{1}{\bar{\rho}_m^2} \int dM_1 M_1 n(M_1, z) \tilde{u}_h(k|M_1, z) \int dM_2 M_2 n(M_2, z) \tilde{u}_h(k|M_2, z) Q(k|M_1, M_2, z). \quad (23)$$

Our treatment of halo exclusion is similar to that of Smith, Scoccimarro & Sheth (2007) and Smith, Desjacques & Marian (2011), except that we have included the (semi-empirical) factor  $\zeta(r, z)$  to account for the radial dependence of halo bias. As shown in Smith et al. (2011), Eq. (23) has the correct asymptotic behavior at both large and small scales. This is an important improvement over a number of *approximate* methods that have been advocated and which typically involve adopting an upper limit for the mass interval used in the integral for the 2-halo term of the power spectrum (e.g., Takada & Jain 2003; Zheng 2004; Abazajian et al. 2005; Tinker et al. 2005, 2012; Yoo et al. 2006; Leauthaud et al. 2011). None of these methods, however, are mathematically correct. Furthermore, accurate, numerical evaluation of Eq. (23) is not significantly more CPU demanding than using the approximate method, largely rescinding its main motivation. Finally, as shown in Smith et al. (2011), Eq. (23) has the additional advantage that it appears to resolve the well-known problem of excess large-scale power in the halo model. This problem arises due to the fact that the 1-halo term approaches a constant value on large scales in Fourier space, significantly in excess of the shot noise (see discussions in Cooray & Sheth 2002; Smith et al. 2003; Crocce & Scoccimarro 2008). A proper treatment of halo exclusion, as adopted here, (almost) nullifies this large scale power of the 1-halo term.

## 2.2 The galaxy-galaxy correlation function

If one assumes that each galaxy resides in a dark matter halo, the halo model described above can also be used to compute the galaxy-galaxy correlation function or the galaxy-matter cross correlation function. All that is needed is a statistical description of how galaxies are distributed over dark matter haloes of different mass. To that extent we use the conditional luminosity function (hereafter CLF) introduced by Yang et al. (2003). The CLF,  $\Phi(L|M)dL$ , specifies the *average* number of galaxies with luminosities in the range  $L \pm dL/2$  that reside in a halo of mass  $M$ .

Throughout we ignore a potential redshift dependence of the CLF. Since the data that we use to constrain the CLF only covers a narrow range in redshift (see Paper III), this assumption will not have a strong impact on our results. Once the CLF is specified, the galaxy luminosity function at redshift  $z$ ,  $\Phi(L, z)$ , simply follows from integrating over the halo mass function,  $n(M, z)$ ;

$$\Phi(L, z) = \int \Phi(L|M) n(M, z) dM. \quad (24)$$

In what follows, we will always be concerned with galaxies in a specific luminosity interval  $[L_1, L_2]$ . The average number density of such galaxies follows from the CLF according to

$$\bar{n}_g(z) = \int \langle N_g|M \rangle n(M, z) dM, \quad (25)$$

where

$$\langle N_g|M \rangle = \int_{L_1}^{L_2} \Phi(L|M) dL, \quad (26)$$

is the average number of galaxies with  $L_1 < L < L_2$  that reside in a halo of mass  $M$ .

For reasons that will become clear below, we split the galaxy population in centrals (defined as those galaxies that reside at the center of their host halo) and satellites (those that orbit around a central), and we split the CLF in two terms accordingly:

$$\Phi(L|M) = \Phi_c(L|M) + \Phi_s(L|M), \quad (27)$$

where  $\Phi_c(L|M)$  and  $\Phi_s(L|M)$  represent central and satellite galaxies, respectively (cf., Cooray & Milosavljevic 2005). Similarly, we write the number density of galaxies,  $n_g(\mathbf{x}, z)$ , as the sum of the contribution of centrals,  $n_c(\mathbf{x}, z)$ , and that of satellites,  $n_s(\mathbf{x}, z)$ , so that

$$\begin{aligned} \delta_g(\mathbf{x}, z) &\equiv \frac{n_g(\mathbf{x}, z) - \bar{n}_g(z)}{\bar{n}_g(z)} \\ &= f_c(z) \delta_c(\mathbf{x}, z) + f_s(z) \delta_s(\mathbf{x}, z). \end{aligned} \quad (28)$$

Here  $f_c(z) = \bar{n}_c(z)/\bar{n}_g(z)$  is the central fraction,  $f_s(z) = \bar{n}_s(z)/\bar{n}_g(z) = 1 - f_c(z)$  is the satellite fraction, and  $\delta_c(\mathbf{x}, z)$  and  $\delta_s(\mathbf{x}, z)$  are the number density contrasts of centrals and satellites at redshift  $z$ , respectively. Note that  $\bar{n}_c(z)$  and  $\bar{n}_s(z)$  simply follow from Eq. (25) by replacing  $\Phi(L|M)$  in Eq. (26) by  $\Phi_c(L|M)$  and  $\Phi_s(L|M)$ , respectively.

The detailed functional form that we adopt for  $\Phi(L|M)$  is discussed in §3.7. In this subsection we show how the CLF enters in the computation of the (projected) galaxy-galaxy correlation function,  $w_p(r_p|L_1, L_2, z)$ , and in the excess surface density profile,  $\Delta\Sigma(R|L_1, L_2, z)$ .

Within the framework of the halo model, we can write

$$n_c(\mathbf{x}, z) = \sum_i \mathcal{N}_{h,i} \mathcal{N}_{c,i} \delta^D(\mathbf{x} - \mathbf{x}_i), \quad (29)$$

where  $\mathcal{N}_{c,i}$  is the number of central galaxies in the halo whose center is in volume element  $i$  (i.e.,  $\mathcal{N}_{c,i}$  is either 0 or 1). The Dirac delta function expresses the fact that a central, by definition, resides at the center of a dark matter halo. Similarly, for the satellite galaxies we can write

$$n_s(\mathbf{x}, z) = \sum_i \mathcal{N}_{h,i} \mathcal{N}_{s,i} u_s(\mathbf{x} - \mathbf{x}_i | M_i, z), \quad (30)$$

where  $\mathcal{N}_{s,i}$  is a positive integer indicating the number of satellite galaxies that reside in the halo whose center is in volume element  $i$ , and  $u_s(r|M, z)$  describes the *normalized* radial distribution of satellite galaxies in an *average* halo of mass  $M$  at redshift  $z$ <sup>‡</sup>.

Using Eq.(28), the galaxy-galaxy power spectrum can be written as

$$P_{\text{gg}}(k, z) = f_c^2(z) P_{\text{cc}}(k, z) + 2f_c(z) f_s(z) P_{\text{cs}}(k, z) + f_s^2(z) P_{\text{ss}}(k, z), \quad (31)$$

while the galaxy-matter cross power spectrum is given by

$$P_{\text{gm}}(k, z) = f_c(z) P_{\text{cm}}(k, z) + f_s(z) P_{\text{sm}}(k, z). \quad (32)$$

Using the same methodology as in §2.1 for the dark matter, we split each of these five power-spectra into a 1-halo and a 2-halo term. The various 2-halo terms are given by

$$P_{\text{xy}}^{2\text{h}}(k, z) = \int dM_1 \mathcal{H}_x(k|M_1, z) n(M_1, z) \int dM_2 \mathcal{H}_y(k|M_2, z) n(M_2, z) Q(k|M_1, M_2, z), \quad (33)$$

where ‘x’ and ‘y’ are either ‘c’ (for central), ‘s’ (for satellite), or ‘m’ (for matter),  $Q(k|M_1, M_2, z)$  is given by Eq. (20), and we have defined

$$\mathcal{H}_m(k, M, z) = \frac{M}{\bar{\rho}_m} \tilde{u}_h(k|M, z), \quad (34)$$

$$\mathcal{H}_c(k, M, z) = \mathcal{H}_c(M, z) = \frac{\langle N_c | M \rangle}{\bar{n}_c(z)}, \quad (35)$$

and

$$\mathcal{H}_s(k, M, z) = \frac{\langle N_s | M \rangle}{\bar{n}_s(z)} \tilde{u}_s(k|M, z). \quad (36)$$

Here  $\langle N_c | M \rangle$  and  $\langle N_s | M \rangle$  are the average number of central and satellite galaxies in a halo of mass  $M$ , which follow from Eq. (26) upon replacing  $\Phi(L|M)$  by  $\Phi_c(L|M)$  and  $\Phi_s(L|M)$ , respectively.

For the 1-halo terms, one obtains

$$P_{\text{cc}}^{1\text{h}}(k, z) = \frac{1}{\bar{n}_c(z)}, \quad (37)$$

<sup>‡</sup> Strictly speaking, by writing  $n_s(\mathbf{x}, z)$  in terms of  $u_s(r|M, z)$  we have already taken an ensemble average over all possible spatial realizations of the satellite galaxies in a halo of mass  $M$  at redshift  $z$ . Hence, the number density distribution of Eq. (30) does not correspond to a single realization, as it should. However, since we are only concerned here with power-spectra, which are anyways based on ensemble averaging, Eq. (30) is adequate for what follows.

$$P_{\text{cs}}^{1\text{h}}(k, z) = \int dM \mathcal{H}_c(M, z) \mathcal{H}_s(k, M, z) n(M, z), \quad (38)$$

and

$$P_{\text{ss}}^{1\text{h}}(k, z) = \mathcal{A}_P \int dM \mathcal{H}_s^2(k, M, z) n(M, z). \quad (39)$$

Here we have assumed that the occupation numbers of centrals and satellites are independent, so that  $\langle N_c N_s | M \rangle = \langle N_c | M \rangle \langle N_s | M \rangle$ , and we have introduced the parameter

$$\mathcal{A}_P \equiv \frac{\langle N_s (N_s - 1) | M \rangle}{\langle N_s | M \rangle^2}. \quad (40)$$

If the occupation number of satellites follows a Poisson distribution, i.e.,

$$P(N_s | M) = \frac{\lambda^{N_s} e^{-\lambda}}{N_s!}, \quad (41)$$

with  $\lambda = \langle N_s | M \rangle$ , then  $\mathcal{A}_P = 1$ , while values of  $\mathcal{A}_P$  larger (smaller) than unity indicate super- (sub-) Poisson statistics.

### 2.3 The Projected Correlation Function and Excess Surface Density

Once  $P_{\text{gg}}(k, z)$  and  $P_{\text{gm}}(k, z)$  have been determined, it is fairly straightforward to compute the projected galaxy-galaxy correlation function,  $w_p(r_p, z)$ , and the excess surface density (ESD) profile,  $\Delta\Sigma(R, z)$ . We start by Fourier transforming the power-spectra to obtain the two-point correlation functions:

$$\begin{aligned} \xi_{\text{xy}}(r, z) &= \frac{1}{(2\pi)^3} \int P_{\text{xy}}(k, z) e^{+i\mathbf{k}\cdot\mathbf{x}} d^3\mathbf{k} \\ &= \frac{1}{2\pi^2} \int_0^\infty P_{\text{xy}}(k, z) \frac{\sin kr}{kr} k^2 dk, \end{aligned} \quad (42)$$

where ‘x’ and ‘y’ are as defined above.

As discussed above, the excess surface density profile

$$\Delta\Sigma(R, z) = \bar{\Sigma}(< R, z) - \Sigma(R, z), \quad (43)$$

where  $\bar{\Sigma}(< R, z)$  is given by Eq. (4). The projected surface density,  $\Sigma(R, z)$ , is related to the galaxy-matter cross correlation,  $\xi_{\text{gm}}(r, z)$ , according to

$$\Sigma(R, z) = \bar{\rho}_m \int_0^{\omega_s} [1 + \xi_{\text{gm}}(r, z)] d\omega, \quad (44)$$

where the integral is along the line of sight with  $\omega$  the comoving distance from the observer. The three-dimensional comoving distance  $r$  is related to  $\omega$  through  $r^2 = \omega_L^2 + \omega^2 - 2\omega_L\omega\cos\theta$ . Here  $\omega_L$  is the comoving distance to the lens, and  $\theta$  is the angular separation between lens and source (see Fig. 1 in Cacciato et al. 2009). Since  $\xi_{\text{gm}}(r, z)$  goes to zero in the limit  $r \rightarrow \infty$ , and since in practice  $\theta$  is small, we can approximate  $\Sigma(R, z)$  using Eq. (3), which is the expression we adopt throughout.

The projected galaxy-galaxy correlation function is defined as

$$w_p(r_p, z) = 2 \int_0^{r_{\text{max}}} \xi_{\text{gg}}(r_p, r_\pi, z) dr_\pi. \quad (45)$$

Here  $r_p$  is the projected separation between two galaxies,  $r_\pi$  is the redshift-space separation along the line-of-sight, and  $\xi_{\text{gg}}(r_p, r_\pi, z)$  is the measured two-dimensional correlation function, which is anisotropic due to the presence of

peculiar velocities. In the limit  $r_{\max} \rightarrow \infty$ , the projected correlation function (45) is completely independent of these peculiar velocities, simply because they have been integrated out. In that case,  $w_p(r_p, z)$  can be written as a simple Abel transform of the real-space correlation function:

$$w_p(r_p, z) = 2 \int_{r_p}^{\infty} \xi_{\text{gg}}(r, z) \frac{r \, dr}{\sqrt{r^2 - r_p^2}}, \quad (46)$$

(Davis & Peebles 1983). However, since real data sets are always limited in extent, in practice the projected correlation function  $w_p(r_p, z)$  is always obtained by integrating  $\xi_{\text{gg}}(r_p, r_\pi, z)$  out to some finite  $r_{\max}$  rather than to infinity. For example, Zehavi et al. (2011), whose data we use in Paper III, adopt  $r_{\max} = 40h^{-1}$  Mpc or  $60h^{-1}$  Mpc, depending on the luminosity sample used. This finite integration range is often ignored in the modeling (e.g., Magliocchetti & Porciani 2003; Collister & Lahav 2005; Wake et al. 2008a,b) or is ‘accounted’ for by computing the model prediction for  $w_p(r_p, z)$  using Eq. (46), but integrating from  $r_p$  out to  $r_{\text{out}} \equiv \sqrt{r_p^2 + r_{\max}^2}$ , where  $r_{\max}$  is the same value as used for the data (e.g., Zehavi et al. 2004, 2005, 2011; Abazajian et al. 2005; Tinker et al. 2005; Zheng et al. 2007, 2009; Yoo et al. 2009). However, as we demonstrate in §4.5 below, this introduces errors that can easily exceed 40 percent or more on the largest scales probed by the data ( $\sim 20h^{-1}$  Mpc; see also Padmanabhan, White & Eisenstein 2007; Norberg et al. 2009; Baldauf et al. 2010). This is due to the fact that the peculiar velocities on scales  $r > r_{\max}$  cannot be ignored. In order to take these residual redshift space distortions into account, we make the assumption that the large scale peculiar velocities are completely dominated by linear velocities (i.e., those that derive from linear perturbation theory), and that the non-linear motions that give rise to the Finger-of-God effect have been integrated out. In that case we can correct Eq. (46) for the fact that the projected correlation function has been obtained using Eq. (45) with a finite  $r_{\max}$  as follows:

$$w_p(r_p, z) = 2 f_{\text{corr}}(r_p, z) \int_{r_p}^{r_{\text{out}}} \xi_{\text{gg}}(r, z) \frac{r \, dr}{\sqrt{r^2 - r_p^2}}, \quad (47)$$

where  $f_{\text{corr}}(r_p, z)$  is the correction factor given by

$$f_{\text{corr}}(r_p, z) = \frac{\int_0^{r_{\max}} \xi_{\text{gg}}^{\text{lin}}(r_p, r_\pi, z) \, dr_\pi}{\int_{r_p}^{r_{\text{out}}} \xi_{\text{gg}}^{\text{lin}}(r, z) \frac{r \, dr}{\sqrt{r^2 - r_p^2}}}. \quad (48)$$

Here  $\xi_{\text{gg}}^{\text{lin}}(r, z)$  and  $\xi_{\text{gg}}^{\text{lin}}(r_p, r_\pi, z)$  are the linear two-point correlation functions of galaxies at redshift  $z$  in real space and redshift space, respectively. For the former we may write

$$\xi_{\text{gg}}^{\text{lin}}(r, z) \equiv \bar{b}^2(z) \xi_{\text{mm}}^{\text{lin}}(r, z), \quad (49)$$

with  $\xi_{\text{mm}}^{\text{lin}}(r, z)$  the two-point correlation function of the initial matter field, linearly extrapolated to redshift  $z$ , and

$$\bar{b}(z) = \frac{1}{\bar{n}_g(z)} \int \langle N_g | M \rangle b_h(M, z) n(M, z) \, dM, \quad (50)$$

is the mean bias of the galaxies in consideration. For the linear galaxy correlation function in redshift space we can write

$$\xi_{\text{gg}}^{\text{lin}}(r_p, r_\pi, z) = \sum_{l=0}^2 \xi_{2l}(s, z) \mathcal{P}_{2l}(\mu) \quad (51)$$

(e.g., Kaiser 1987; Hamilton 1992). Here  $s = \sqrt{r_p^2 + r_\pi^2}$  is the separation between the galaxies in redshift space,  $\mu = r_\pi/s$  is the cosine of the line-of-sight angle,  $\mathcal{P}_l(x)$  is the  $l^{\text{th}}$  Legendre polynomial, and  $\xi_0$ ,  $\xi_2$ , and  $\xi_4$  are given by

$$\xi_0(r, z) = \left(1 + \frac{2}{3}\beta + \frac{1}{5}\beta^2\right) \xi_{\text{gg}}^{\text{lin}}(r, z), \quad (52)$$

$$\xi_2(r, z) = \left(\frac{4}{3}\beta + \frac{4}{7}\beta^2\right) [\xi_{\text{gg}}^{\text{lin}}(r, z) - 3J_3(r, z)], \quad (53)$$

$$\xi_4(r, z) = \frac{8}{35}\beta^2 \left[\xi_{\text{gg}}^{\text{lin}}(r, z) + \frac{15}{2}J_3(r, z) - \frac{35}{2}J_5(r, z)\right], \quad (54)$$

where

$$J_n(r, z) = \frac{1}{r^n} \int_0^r \xi_{\text{gg}}^{\text{lin}}(y, z) y^{n-1} \, dy. \quad (55)$$

and

$$\beta = \beta(z) = \frac{1}{\bar{b}(z)} \left( \frac{d \ln D}{d \ln a} \right)_z \simeq \frac{\Omega_m^{0.6}(z)}{\bar{b}(z)} \quad (56)$$

with  $a = 1/(1+z)$  the scale factor and  $D(z)$  the linear growth rate.

As we demonstrate in §4.5, although this correction is fairly accurate on large scales ( $\gtrsim 3h^{-1}$  Mpc), on smaller scales it introduces an error of a few percent (see also Baldauf et al. 2010). Detailed tests with mocks indicate that this problem can be avoided by simply replacing the linear galaxy-galaxy correlation function in the Kaiser formalism with its non-linear analog; i.e., by replacing in Eq. (48) and Eqs. (52)-(55) each occurrence of  $\xi_{\text{gg}}^{\text{lin}}(r, z)$  with  $\xi_{\text{gg}}(r, z)$  computed from Eq. (42) using the model outlined in §2.2. This is the method we will use throughout whenever we compute  $w_p(r_p, z)$  for comparison with data, always using the same  $r_{\max}$  as used for the data (see Paper III) and with  $\bar{b}(z)$  computed from our CLF model using Eq. (50). Note that with this modified version of the Kaiser formalism, the denominator of  $f_{\text{corr}}$  in Eq. (48) is exactly equal to the integral in Eq. (47). Hence, there is no need to compute the correction factor; rather,  $w_p(r_p, z)$  can simply be obtained directly using Eq. (45) with  $\xi_{\text{gg}}(r_p, r_\pi, z)$  given by Eqs. (51)-(55), but with  $\xi_{\text{gg}}^{\text{lin}}(r, z)$  replaced by  $\xi_{\text{gg}}(r, z)$  (see §4.5 for details).

### 3 MODEL INGREDIENTS

The model described in the previous section requires a number of ingredients, namely the halo mass function,  $n(M, z)$ , the halo bias function,  $b_h(M, z)$ , the radial bias function,  $\zeta(r, z)$ , the linear and non-linear matter power spectra,  $P_{\text{mm}}^{\text{lin}}(k, z)$  and  $P_{\text{mm}}(k, z)$ , respectively, the (normalized) halo density profile,  $u_h(r|M)$ , the (normalized) radial number density distribution of satellite galaxies,  $u_s(r|M)$ , and the halo occupations statistics  $\langle N_c | M \rangle$  and  $\langle N_s | M \rangle$ . We now discuss these ingredients in turn.

#### 3.1 Matter Power Spectra

In our fiducial model, which includes a treatment of halo exclusion, we require both the linear and the non-linear two-point correlation functions of the matter,  $\xi_{\text{mm}}^{\text{lin}}(r, z)$  and  $\xi_{\text{mm}}(r, z)$ , which are the Fourier transform of the linear and non-linear power-spectrum,  $P_{\text{mm}}^{\text{lin}}(k, z)$  and  $P_{\text{mm}}(k, z)$ , respectively.

Throughout we compute  $P_{\text{mm}}(k, z)$  using the fitting formula of Smith et al. (2003)<sup>§</sup> which is modeled on the basis of the *linear* matter power spectrum,

$$P_{\text{mm}}^{\text{lin}}(k, z) \propto D^2(z) T^2(k) k^{n_s}. \quad (57)$$

Here  $n_s$  is the spectral index of the initial power spectrum,  $T(k)$  is the linear transfer function, and  $D(z)$  is the linear growth factor at redshift  $z$ , normalized to unity at  $z = 0$ . We adopt the linear transfer function of Eisenstein & Hu (1998), which properly accounts for the baryons, neglecting any contribution from neutrinos and assuming a CMB temperature of 2.725K (Mather et al. 1999). The power spectrum is normalized such that the mass variance

$$\sigma^2(M) = \frac{1}{2\pi^2} \int P_{\text{mm}}^{\text{lin}}(k, 0) \widetilde{W}^2(kR) k^2 dk, \quad (58)$$

is equal to  $\sigma_8^2$  for  $R = 8h^{-1}$  Mpc. Here

$$\widetilde{W}(kR) = \frac{3(\sin kR - kR \cos kR)}{(kR)^3}, \quad (59)$$

is the Fourier transform of the spatial top-hat filter, and  $M$  is related to  $R$  according to  $M = 4\pi\bar{\rho}_m R^3/3$ .

### 3.2 Halo Mass Function

For the halo mass function,  $n(M, z)$ , which specifies the comoving abundance of dark matter haloes of mass  $M$  at redshift  $z$ , we use the results of Tinker et al. (2008, 2010), who have shown that the halo mass function is accurately described by

$$n(M, z) = \frac{\bar{\rho}_m}{M^2} \nu f(\nu) \frac{d \ln \nu}{d \ln M}, \quad (60)$$

where  $\nu = \delta_{\text{sc}}(z)/\sigma(M)$ , with  $\delta_{\text{sc}}(z)$  the critical overdensity required for spherical collapse at  $z$ , and

$$f(\nu) = \eta_0 [1 + (\eta_1 \nu)^{-2\eta_2}] \nu^{2\eta_3} e^{-\eta_4 \nu^2/2}. \quad (61)$$

For our definition of halo mass (see §2.1), Tinker et al. (2010) find that  $\eta_1 = 0.589(1+z)^{0.20}$ ,  $\eta_2 = -0.729(1+z)^{-0.08}$ ,  $\eta_3 = -0.243(1+z)^{0.27}$ , and  $\eta_4 = 0.864(1+z)^{-0.01}$ , while  $\eta_0 = \eta_0(z)$  is set by the normalization condition

$$\int b_h(\nu) f(\nu) d\nu = 1, \quad (62)$$

with  $b_h(\nu)$  the halo bias function of Tinker et al. (2010), specified in §3.3 below. This normalization expresses that the distribution of matter is, by definition, unbiased with respect to itself.

Throughout we adopt

$$\delta_{\text{sc}}(z) = 0.15 (12\pi)^{2/3} \frac{[\Omega_m(z)]^{0.0055}}{D(z)}, \quad (63)$$

which is a good numerical approximation to the critical threshold for spherical collapse (Navarro, Frenk & White 1997).

<sup>§</sup> We use the small modification suggested on John Peacock's website <http://www.roe.ac.uk/~jap/haloes/>, although it has no significant impact on any of our results.

### 3.3 Halo Bias Function

For the halo bias function we adopt the fitting function of Tinker et al. (2010), which for our definition of halo mass, can be written as

$$b_h(M, z) = b_h(\nu) = 1 - \frac{\nu^{0.1325}}{\nu^{0.1325} + 1.0716} + 0.1830\nu^{1.5} + 0.2652\nu^{2.4} \quad (64)$$

where, as before,  $\nu = \delta_{\text{sc}}(z)/\sigma(M)$ ,

Although we believe the halo mass function and halo bias function obtained by Tinker et al. (2008, 2010) to be the most accurate to date, it is important to realize that they still can carry uncertainties that can potentially impact cosmological results. It is unclear if such uncertainties affect just the mass function normalization and not its shape. We will carry out a proper investigation of this issue in future work. Throughout this paper, however, we restrict ourselves to the  $n(M, z)$  and  $b_h(M, z)$  specified above.

### 3.4 Radial Bias Function

An important ingredient of the halo model is the radial bias function,  $\zeta(r, z)$ , which accounts for the fact that Eq. (10) becomes inaccurate in the quasi-linear regime, by making halo bias scale dependent, i.e., it effectively describes the impact of the non-zero higher-order bias factors in Eq. (9).

Ideally, the radial dependence of the halo bias is to be computed from first principles using, for example, (renormalized) perturbation theory (e.g., Crocce & Scoccimarro 2006; McDonald 2006, 2007; Smith, Scoccimarro & Sheth 2007; Elia et al. 2011). However, it remains to be seen whether these techniques can yield reliable results in the quasi-linear regime of the 1-halo to 2-halo transition region, which will probably require an impracticable large number of orders or loops in the perturbation series. In the absence of such an analytical solution we have to resort to empirical fitting functions calibrated against numerical simulations. Throughout, we adopt the fitting function of Tinker et al. (2005), given by

$$\zeta_0(r, z) = \frac{[1 + 1.17 \xi_{\text{mm}}(r, z)]^{1.49}}{[1 + 0.69 \xi_{\text{mm}}(r, z)]^{2.09}}. \quad (65)$$

The subscript 0 indicates that this fitting function was calibrated using  $N$ -body simulations in which the haloes were identified using the friends-of-friends (FOF) percolation algorithm (e.g., Davis et al. 1985), with a linking length of 0.2 times the mean inter-particle separation. However, the halo mass function and halo bias function used here are based on the spherical overdensity algorithm. As already pointed out in Appendix A of Tinker et al. (2012), because of these different halo definitions, the fitting function (65) is likely to be inadequate on small scales, which we indeed find to be the case (see §4.2 below). After some trial and error, while assuring an easy numerical implementation, we decided to adopt the following, modified, radial bias function

$$\zeta(r, z) = \begin{cases} \zeta_0(r, z) & \text{if } r \geq r_\psi \\ \zeta_0(r_\psi, z) & \text{if } r < r_\psi \end{cases} \quad (66)$$

where the characteristic radius,  $r_\psi$ , is defined by

$$\log [\zeta_0(r_\psi, z) \xi_{\text{mm}}(r_\psi, z)] = \psi \quad (67)$$



where  $\psi$  is a free parameter to be calibrated against numerical simulations (see §4.2). Note that if Eq. (67) has no solution, e.g., when  $\psi \rightarrow +\infty$ , we set  $r_\psi = 0$ , which corresponds to simply using the fitting function (65) without modification.

### 3.5 Density Profile of Dark Matter Haloes

We assume that dark matter haloes are spheres whose normalized density distribution is given by the NFW profile

$$u_h(r|M) = \frac{\bar{\rho}_m}{M} \frac{\delta_{200}}{(r/r_*)(1+r/r_*)^2}, \quad (68)$$

(Navarro, Frenk & White 1997), where  $r_*$  is a characteristic radius and  $\delta_{200}$  is a dimensionless amplitude which can be expressed in terms of the halo concentration parameter  $c \equiv r_{200}/r_*$  as

$$\delta_{200} = \frac{200}{3} \frac{c^3}{\ln(1+c) - c/(1+c)}. \quad (69)$$

Numerical simulations show that  $c$  is correlated with halo mass. Throughout our work we use the concentration-mass relation of Macciò et al. (2007), properly converted to our definition of halo mass.

The Fourier transform of the NFW profile, which features predominantly in our model, is given by

$$\begin{aligned} \tilde{u}_h(k|M, z) &= \frac{3\delta_{200}}{200c^3} \left( \cos \mu [\text{Ci}(\mu + \mu c) - \text{Ci}(\mu)] + \right. \\ &\quad \left. \sin \mu [\text{Si}(\mu + \mu c) - \text{Si}(\mu)] - \frac{\sin \mu c}{\mu + \mu c} \right), \end{aligned} \quad (70)$$

where  $\mu \equiv kr_*$ , and  $\text{Si}(x)$  and  $\text{Ci}(x)$  are the standard sine and cosine integrals, respectively.

Note that this model for dark matter haloes is highly oversimplified. In reality, haloes are triaxial, rather than spherical, have scatter in the concentration-mass relation, have substructure, and may have a density profile that differs significantly from a NFW profile due to the action of baryons. A detailed discussion regarding the impact of these oversimplifications on our results is presented in §5.

### 3.6 Radial Number Density Distribution of Satellites

Throughout, we assume that satellite galaxies follow a radial number density distribution given by a generalized NFW profile (e.g., van den Bosch et al. 2004):

$$u_s(r|M) \propto \left( \frac{r}{\mathcal{R}r_*} \right)^{-\gamma} \left( 1 + \frac{r}{\mathcal{R}r_*} \right)^{\alpha-3}, \quad (71)$$

so that  $u_s \propto r^{-\gamma}$  and  $u_s \propto r^{-3}$  at small and large radii, respectively. Here  $\mathcal{R}$  and  $\gamma$  are two free parameters, while the scale radius  $r_*$  is the same as that for the dark matter mass profile (Eq. [68]). For our fiducial model, we adopt  $\mathcal{R} = \gamma = 1$  so that  $u_s(r|M) = u_h(r|M)$ , i.e. satellites are unbiased with respect to the dark matter. For consistency with our definition of halo mass, we only adopt profile (71) out to  $r_{200}$  (i.e., all satellites have halo-centric radii  $r < r_{200}$ ).

Observations of the number density distribution of satellite galaxies in clusters and groups seem to suggest that  $u_s(r|M)$  is in reasonable agreement with an NFW profile, for which  $\gamma = 1$  (e.g., Beers & Tonry 1986; Carlberg, Yee

& Ellingson 1997a; van der Marel et al. 2000; Lin, Mohr & Stanford 2004; van den Bosch et al. 2005a). However, several studies have suggested that the satellite galaxies are less centrally concentrated than the dark matter, corresponding to  $\mathcal{R} > 1$  (e.g., Yang et al. 2005; Chen 2008; More et al. 2009a). On the other hand, in the case of very massive galaxies, in particular luminous red galaxies, there are strong indications that they follow a radial profile that is *more* centrally concentrated (i.e.,  $\mathcal{R} < 1$ ) than the dark matter (e.g., Masjedi et al. 2006; Watson et al. 2010, 2012; Tal, Wake & van Dokkum 2012). In Paper III we therefore examine how the results depend on changes in  $\mathcal{R}$ .

### 3.7 Halo Occupation Statistics

As specified in §2.2, the halo occupation statistics  $\langle N_c|M \rangle$  and  $\langle N_s|M \rangle$ , required to describe the galaxy auto-correlation function and the galaxy-matter cross-correlation function, are obtained from the CLF,

$$\Phi(L|M) = \Phi_c(L|M) + \Phi_s(L|M), \quad (72)$$

We use the CLF model presented in Cacciato et al. (2009), which is motivated by the CLFs obtained by Yang, Mo & van den Bosch (2008) from a large galaxy group catalog (Yang et al. 2007) extracted from the SDSS Data Release 4 (Adelman-McCarthy et al. 2006). In particular, the CLF of central galaxies is modeled as a log-normal:

$$\Phi_c(L|M) dL = \frac{\log e}{\sqrt{2\pi}\sigma_c} \exp \left[ -\frac{(\log L - \log L_c)^2}{2\sigma_c^2} \right] \frac{dL}{L}, \quad (73)$$

and the satellite term as a modified Schechter function:

$$\Phi_s(L|M) dL = \phi_s^* \left( \frac{L}{L_s^*} \right)^{\alpha_s+1} \exp \left[ -\left( \frac{L}{L_s^*} \right)^2 \right] \frac{dL}{L}, \quad (74)$$

which decreases faster than a Schechter function at the bright end. Note that  $L_c$ ,  $\sigma_c$ ,  $\phi_s^*$ ,  $\alpha_s$  and  $L_s^*$  are all functions of the halo mass  $M$ .

Following Cacciato et al. (2009), and motivated by the results of Yang et al. (2008) and More et al. (2009a, 2011), we assume that  $\sigma_c$ , which expresses the scatter in  $\log L$  of central galaxies at fixed halo mass, is a constant (i.e. is independent of halo mass and redshift). In addition, for  $L_c$ , which is defined such that  $\log L_c$  is the expectation value for the (10-based) logarithm of the luminosity of a central galaxy, i.e.

$$\log L_c = \int_0^\infty \Phi_c(L|M) \log L dL, \quad (75)$$

we adopt the following parameterization;

$$L_c(M) = L_0 \frac{(M/M_1)^{\gamma_1}}{[1 + (M/M_1)]^{\gamma_1 - \gamma_2}}. \quad (76)$$

Hence,  $L_c \propto M^{\gamma_1}$  for  $M \ll M_1$  and  $L_c \propto M^{\gamma_2}$  for  $M \gg M_1$ . Here  $M_1$  is a characteristic mass scale, and  $L_0 = 2^{\gamma_1 - \gamma_2} L_c(M_1)$  is a normalization.

For the satellite galaxies we adopt

$$L_s^*(M) = 0.562 L_c(M), \quad (77)$$

$$\alpha_s(M) = \alpha_s \quad (78)$$

and

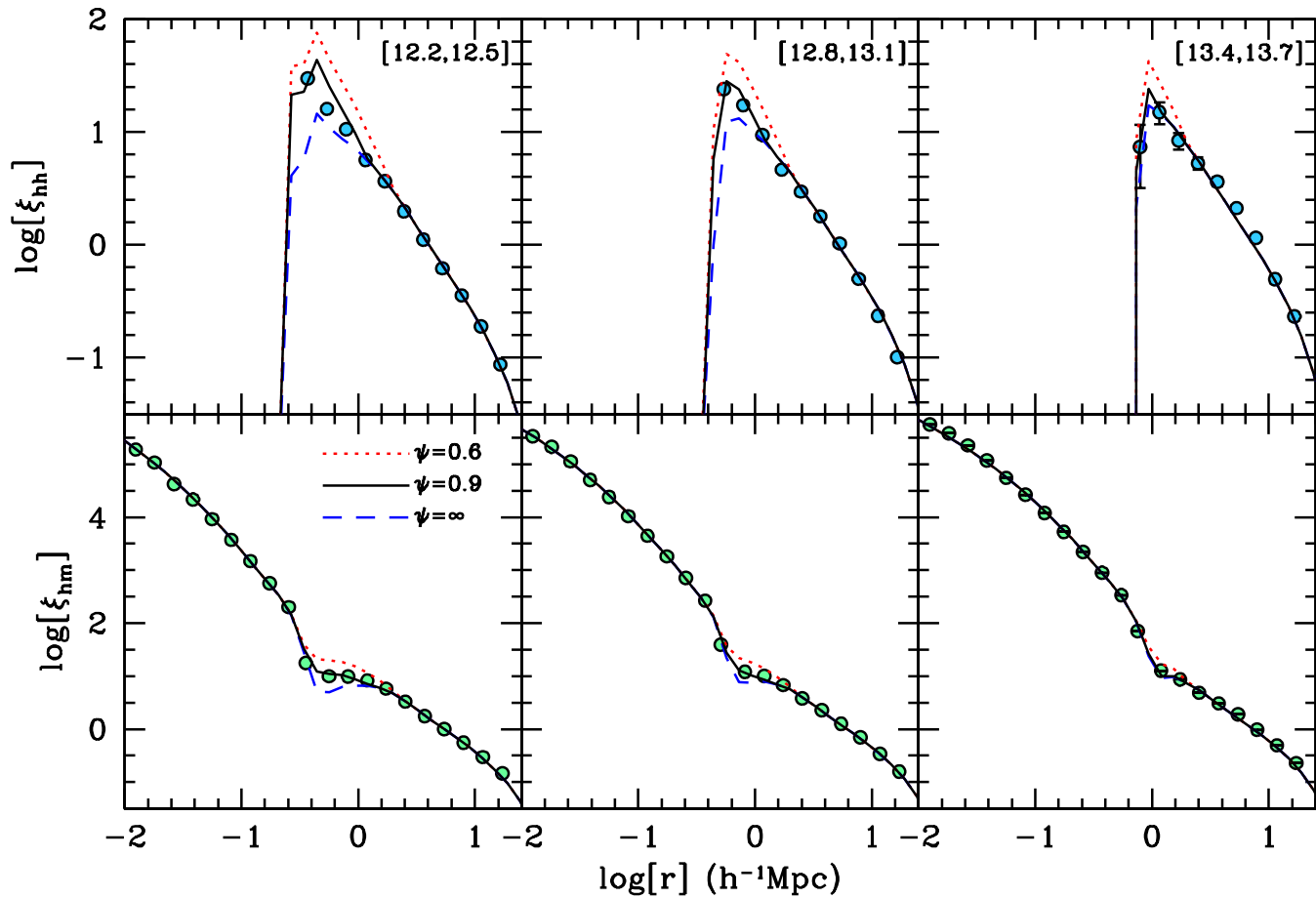


**Figure 1.** The halo-halo (top panels) and halo-matter (bottom panels) two-point correlation functions for haloes in three mass bins, as indicated in the top panels [values in square brackets indicate  $\log(M/(h^{-1} M_{\odot}))$ ]. Colored symbols reflect the results obtained from the L250 simulation box. Errorbars (from Poisson statistics) are indicated, but since they are almost always smaller than the symbols, they can only be seen for 2 or 3 data points. The various curves are analytical results for three different values of  $\psi$ , as indicated in the lower left-hand panel. Note that the model with  $\psi = 0.9$  accurately reproduces the sharp feature in  $\xi_{\text{hm}}(r)$ , which reflects the 1-halo to 2-halo transition regime.

$$\log[\phi_s^*(M)] = b_0 + b_1(\log M_{12}) + b_2(\log M_{12})^2, \quad (79)$$

with  $M_{12} = M/(10^{12} h^{-1} M_{\odot})$ . Note that neither of these functional forms has a physical motivation; they merely were found to adequately describe the results obtained by Yang et al. (2008) from the SDSS galaxy group catalog.

Our parameterization of the CLF thus has a total of nine free parameters

$$\lambda_{\text{CLF}} \equiv (\log M_1, \log L_0, \gamma_1, \gamma_2, \sigma_c, \alpha_s, b_0, b_1, b_2) \quad (80)$$

The final parameter used to describe the halo occupation statistics of the galaxies is  $\mathcal{A}_{\text{P}}$ , defined in Eq. (39). In our fiducial model, adopted here, we will keep this parameter fixed at  $\mathcal{A}_{\text{P}} = 1$ , which corresponds to assuming that satellites follow Poisson statistics. As shown in Yang et al. (2008), this assumption has strong support from galaxy group catalogs. Additional support comes from numerical simulations which show that dark matter subhaloes (which are believed to host satellite galaxies) also follow Poisson statistics (Kravtsov et al. 2004). However, there are also some indications that the occupation statistics of subhaloes and/or satellite galaxies are actually slightly super-Poisson, i.e.,  $\mathcal{A}_{\text{P}} \gtrsim 1$  (e.g., Porciani, Magliocchetti & Norberg 2004;

Giocoli et al. 2010a; Busha et al. 2011; Boylan-Kolchin et al. 2010). Hence, in Paper III we will also discuss models in which  $\mathcal{A}_{\text{P}}$  is taken to be a free parameter.

## 4 MODEL TESTS

In this section we describe the construction of large mock galaxy distributions, which we use to calibrate and test the real-space galaxy-galaxy and galaxy-matter correlation functions computed using the method outlined in §2.2. In particular, we calibrate the scale dependence of the halo bias and test the accuracy of our halo-exclusion treatment, which we compare to some approximate methods that do not account for halo exclusion but that are frequently used in the literature. In addition, we also use these mock galaxy distributions to test our correction for residual redshift space distortions.

### 4.1 Construction of Mock Galaxy Distributions

For testing and calibrating the method described in §2 we use two different  $N$ -body simulations that have been run us-

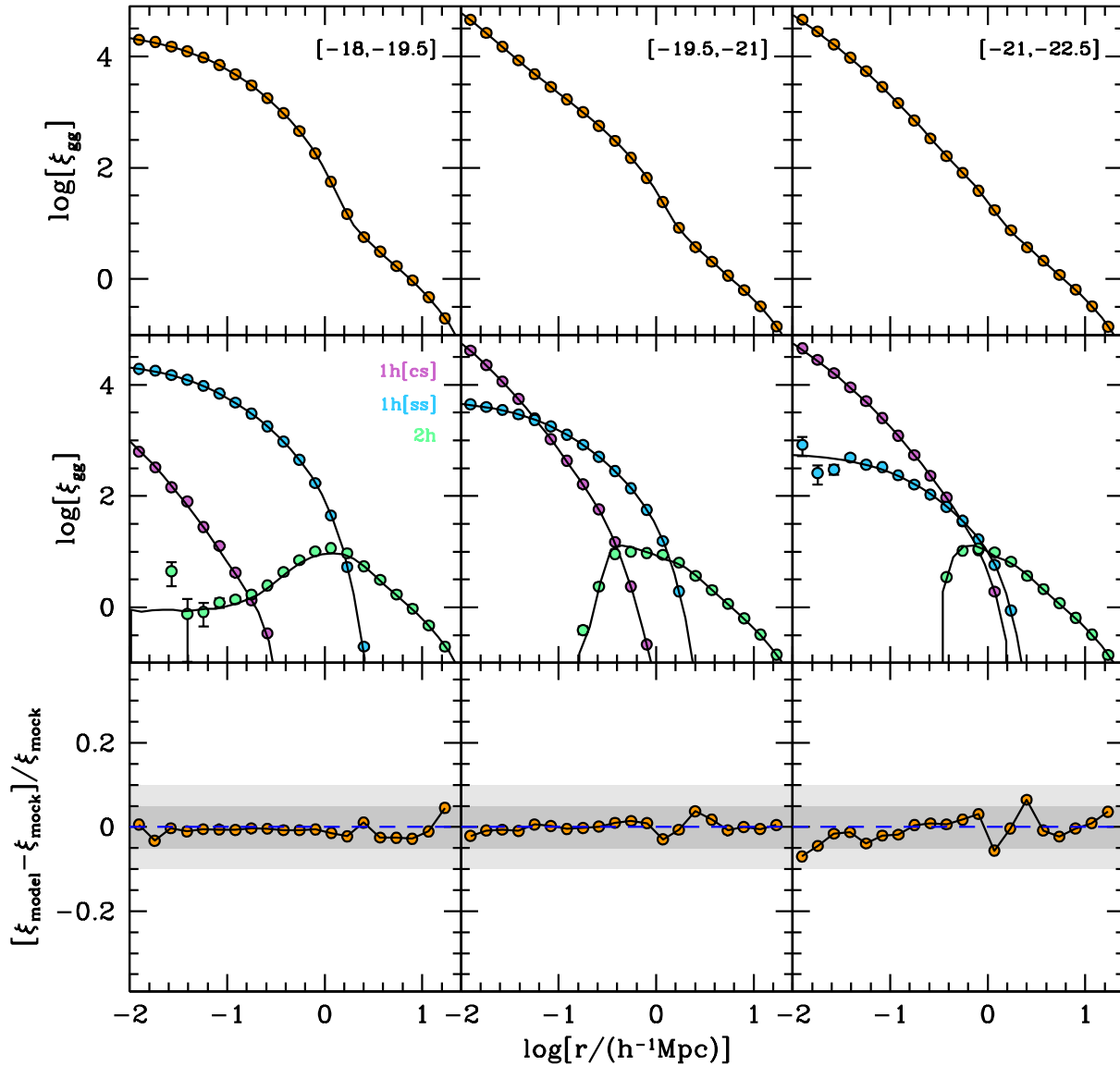


**Figure 2.** Top panels show the galaxy-galaxy two-point correlation functions for three different magnitude bins, as indicated in the top panels [values in square brackets indicate  $^{0.1}M_r - 5 \log h$ ]. Colored symbols reflect the results obtained from the mock galaxy distribution in the L250 simulation box, while the solid line is the prediction of our analytical model. The middle panels show the contributions from the 1-halo central-satellite term (purple symbols, labeled ‘1h[cs]’), the 1-halo satellite-satellite term (blue symbols, labeled ‘1h[ss]’), and the 2-halo term (green symbols, labeled ‘2h’). Once again, the solid lines show the model predictions. As in Fig. 1, errorbars reflecting Poisson statistics are indicated, but are almost always smaller than the symbols. The bottom panels, show the fractional difference between model and mock for the total correlation functions shown in the top panels. The dark and light shaded areas indicate fractional errors of less than 5 and 10 percent, respectively. As is evident, the accuracy of our model is typically better than 5 percent, and always better than 10 percent.

ing the adaptive refinement technique (ART) of Kravtsov, Klypin & Khokhlov (1997). Both simulations have been used by Tinker et al. (2008, 2010) in their studies of the halo mass function and halo bias function, where they are called L250 and L1000W. We adopt the same nomenclature in what follows.

Simulation L250 follows the evolution of  $512^3$  dark matter particles in a cubic box of  $250h^{-1}$  Mpc size in a flat  $\Lambda$ CDM cosmology with matter density  $\Omega_m = 0.3$ , baryon density  $\Omega_b = 0.04$ , Hubble parameter  $h = 0.7$ , spectral index  $n_s = 1.0$ , and a matter power spectrum normalization of  $\sigma_8 = 0.9$ . Simulation L1000W follows the evolution of

$1024^3$  dark matter particles in a  $1h^{-1}$  Gpc size box in a flat  $\Lambda$ CDM cosmology with matter density  $\Omega_m = 0.27$ , baryon density  $\Omega_b = 0.044$ , Hubble parameter  $h = 0.7$ , spectral index  $n_s = 0.95$ , and a matter power spectrum normalization of  $\sigma_8 = 0.79$ . The particle masses are  $m_p = 9.69 \times 10^9 h^{-1} M_\odot$  and  $m_p = 6.98 \times 10^{10} h^{-1} M_\odot$  for L250 and L1000W, respectively.

For both simulations we use the halo catalogs at  $z = 0$ , kindly provided to us by Jeremy Tinker. These haloes are defined as spheres with an overdensity of 200, which is identical to our definition of halo mass (see §2.1). More

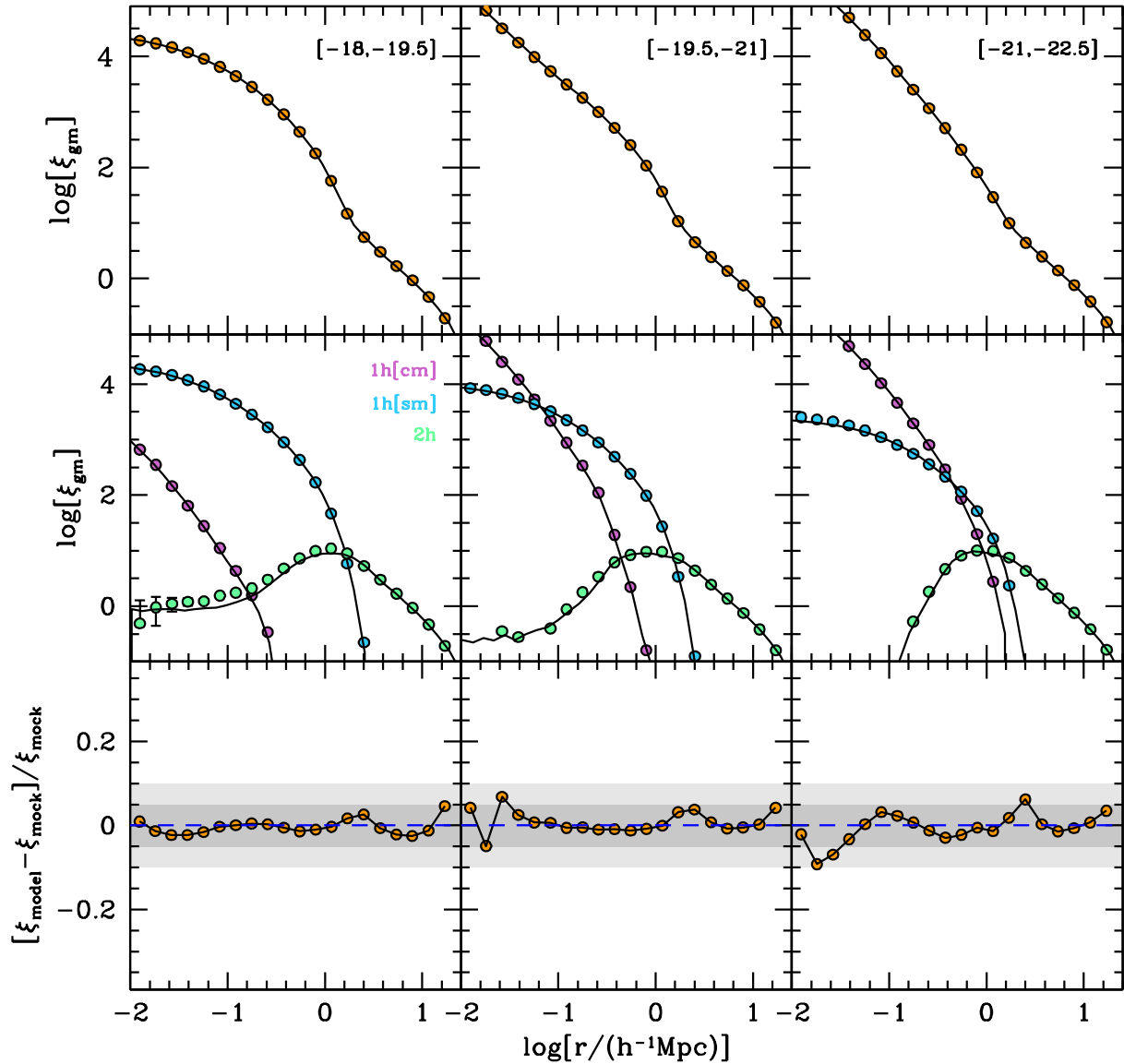


**Figure 3.** Same as Fig. 2 but now for the galaxy-matter cross correlations. In the middle row of panels, the 1-halo component is split in the central-matter (purple symbols, labeled ‘1h[cm]’) and satellite-matter (blue symbols, labeled ‘1h[sm]’) parts. Similar to the galaxy-galaxy correlation functions, the accuracy of our model is typically better than 5 percent, and always better than 10 percent.

information about these simulations and the identification of its dark matter haloes can be found in Tinker et al. (2008).

In what follows we will use the L250 simulation box to calibrate and test our galaxy-galaxy and galaxy-matter correlation functions, while L1000W is used to test our correction for residual redshift space distortions. To this end, we construct mock galaxy distributions by populating the dark matter haloes with model galaxies using the CLF. In particular, we model the CLF using the parameterization described in §3.7 with the following parameters:  $L_0 = 10^{9.9} h^{-2} L_\odot$ ,  $M_1 = 10^{10.9} h^{-1} M_\odot$ ,  $\sigma_c = 0.16$ ,  $\gamma_1 = 5.0$ ,  $\gamma_2 = 0.24$ ,  $\alpha_s = -1.3$ ,  $b_0 = -1.2$ ,  $b_1 = 1.4$ , and  $b_2 = -0.17$ . For each halo we first draw the luminosity of its central galaxy from  $\Phi_{\text{cen}}(L|M)$ , given by Eq. (73). Next, we draw the number of satellite galaxies, under the assumption that  $P(N_{\text{sat}}|M)$  follows a Poisson distribution (i.e.,  $\mathcal{A}_P = 1.0$ ) with mean

$$\langle N_{\text{sat}}|M \rangle = \int_{L_{\text{min}}}^{\infty} \Phi_{\text{sat}}(L|M) dL, \quad (81)$$

where we adopt a luminosity threshold,  $L_{\text{min}}$ , corresponding to  $^{0.1}M_r - 5 \log h = -18$  (here  $^{0.1}M_r$  indicates the SDSS  $r$ -band magnitude,  $K$ -corrected to  $z = 0.1$ ; see Blanton et al. 2003). For each of the  $N_{\text{sat}}$  satellites in the halo of question we then draw a luminosity from the satellite CLF  $\Phi_{\text{sat}}(L|M)$ , given by Eq. (74).

Having assigned all mock galaxies their luminosities, the next step is to assign them a position and velocity within their halo. We assume that the central galaxy resides at rest at the center of the halo, while satellite galaxies follow a spherically symmetric number-density distribution proportional to Eq. (71) with  $\mathcal{R} = \gamma = 1$ , i.e. we assume that satellite galaxies are unbiased with respect to the dark matter. For the halo concentrations we adopt the concentration-mass relation of Macciò et al. (2007), properly converted

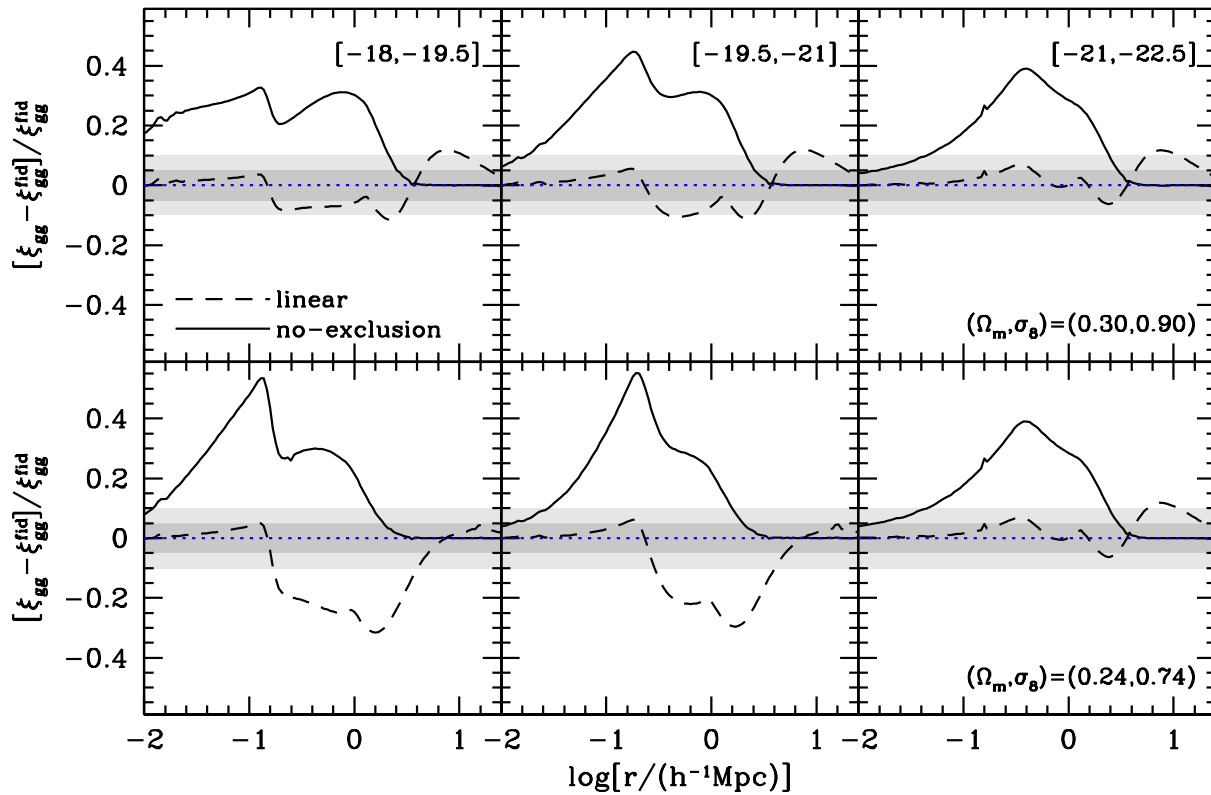


**Figure 4.** The fractional errors of the approximate ‘no-exclusion’ model (solid lines) and ‘linear’ model (dashed lines). Results are shown for three magnitude bins, as indicated, and for two different cosmologies+CLF. In the upper panels we use the same cosmology and CLF as for the mocks in Figs. 1 - 3; in the lower panels we use the WMAP3 cosmology and the corresponding best-fit CLF model of Cacciato et al. (2009). The dark and light shaded areas indicate fractional errors of less than 5 and 10 percent, respectively. Note that both the ‘no-exclusion’ model and the ‘linear’ model have fractional errors that can easily exceed 30-40 percent, which is inadequate for precision cosmology.

to our definition of halo mass. Finally, the peculiar velocities of the satellite galaxies are assigned as follows. We assume that satellite galaxies are in a steady-state equilibrium within their dark matter potential well with an isotropic distribution of velocities with respect to the halo center. One dimensional velocities are drawn from a Gaussian

$$f(v_j) = \frac{1}{\sqrt{2\pi} \sigma_{\text{sat}}(r)} \exp\left[-\frac{v_j^2}{2\sigma_{\text{sat}}^2(r)}\right], \quad (82)$$

with  $v_j$  the velocity relative to that of the central galaxy along axis  $j$  and  $\sigma_{\text{sat}}(r)$  the local, one-dimensional velocity dispersion obtained from solving the Jeans equation (see van den Bosch et al. 2004; More et al. 2009b).

For reasons that will become clear below, in both simulation boxes we only populate dark matter haloes with masses in the range  $M_{\text{min}} \leq M \leq M_{\text{max}}$ , where  $M_{\text{min}} = 10^{12} h^{-1} M_{\odot}$  and  $10^{13} h^{-1} M_{\odot}$  for L250 and L1000W, respectively, while  $M_{\text{max}} = 10^{14.5} h^{-1} M_{\odot}$  for both L250 and L1000W.

## 4.2 Calibrating Scale Dependence of Halo Bias

As discussed in §3.4, fitting function (65) for the radial bias is likely to be inaccurate on small scales due to the fact that it was calibrated for a different halo definition than the one used here. To investigate the magnitude of this effect, and

to test plausible corrections for it, we compare our model predictions against the L250 simulation box.

We start by computing both the halo-halo auto-correlation function,  $\xi_{\text{hh}}(r|M)$  and the halo-matter cross-correlation function,  $\xi_{\text{hm}}(r|M)$ , for a number of bins in halo mass. We only consider haloes in the mass range  $10^{12} h^{-1} M_{\odot} \leq M \leq 10^{14.5} h^{-1} M_{\odot}$ . The lower limit is needed to account for the fact that the simulation has a finite mass resolution, while the upper limit is adopted to be less sensitive to cosmic variance originating from the relatively small volume of the simulation box. Over the mass range  $10^{12} h^{-1} M_{\odot} \leq M \leq 10^{14.5} h^{-1} M_{\odot}$  the halo mass function is in excellent agreement with the fitting function of Tinker et al. (2008), which is also the one used in our analytical calculations. Note that when cross-correlating the haloes with the dark matter particles, we only consider the particles associated with haloes in the mass range  $10^{12} h^{-1} M_{\odot} \leq M \leq 10^{14.5} h^{-1} M_{\odot}$ : A large fraction of all dark matter particles in the simulation box are not associated with any dark matter halo, but that is simply a manifestation of the limited (mass and force) resolution of the  $N$ -body simulation. In other words, the L250 simulation does not properly resolve (non-linear) structure on a mass scale  $M < 10^{12} h^{-1} M_{\odot}$ , and we therefore do not expect our model to accurately reproduce the halo-matter cross correlation function of the simulation if the cross correlation is with *all* dark matter.

The resulting  $\xi_{\text{hh}}(r|M)$  and  $\xi_{\text{hm}}(r|M)$  are shown as filled circles in the upper and lower panels of Fig. 1, respectively. The blue, dashed lines are our model results, which are obtained using the same model as for the galaxy-galaxy and galaxy-matter correlation functions described in §2.2, but by setting  $\langle N_c|M \rangle = 1$  if the halo mass  $M$  falls within the halo mass bin in consideration, and  $\langle N_c|M \rangle = 0$  otherwise, plus  $\langle N_s|M \rangle = 0$  for all  $M$ . Note that all integrals over halo mass are only integrated over the range  $10^{12}h^{-1} M_\odot \leq M \leq 10^{14.5}h^{-1} M_\odot$ . Also, when Fourier transforming the power-spectrum to obtain the correlation function, we adopt a lower limit for the wavenumbers in order to account for the fact that the simulation box has a finite size and periodic boundary conditions: specifically, in Eq. (42) we replace the lower limit of the integration range by  $k_{\text{min}} = \sqrt{3} \times (2\pi/L_{\text{box}})$ . In this model we have set  $\psi = +\infty$ , which implies that we have simply adopted the radial bias function of Tinker et al. (2005) without any modification (i.e.,  $\zeta(r, z) = \zeta_0(r, z)$ ; see §3.4).

The model accurately fits the halo-matter cross correlation functions on both small and large scales. The former indicates that our modeling of the halo density profiles,  $u(r|M)$ , is accurate (i.e., we are not making a significant error because we do not account for halo triaxiality, halo substructure and scatter in halo concentration; see §3.5), while the good fit on large scales argues that our treatment of halo bias is adequate. However, the model clearly underpredicts  $\xi_{\text{hm}}(r)$  at the 1-halo to 2-halo transition regime, which is especially conspicuous in the lower mass bin (lower left-hand panel of Fig. 1). The upper panels clearly indicate that this is a reflection of the fact that the model underpredicts the halo-halo correlation function on small scales ( $\sim 1h^{-1}$  Mpc; just before halo exclusion sets in). The solid and dotted lines are models in which we have used our modified version of the radial bias function (Eq. [66]) with  $\psi = 0.9$  and  $0.6$ , respectively. The former provides the best-fit overall; it somewhat overpredicts the halo-halo correlation function on small scales in the lowest mass bin, but results in excellent fits to the other correlation functions. The model with  $\psi = 0.6$ , on the other hand, clearly overpredicts the small scale clustering of the dark matter haloes for all mass bins. Detailed tests, including additional halo mass bins and other functional forms for a modified  $\zeta(r, z)$ , indicate that Eq. (66) with  $\psi = 0.9$  yield the best results, while still allowing for a sufficiently fast numerical evaluation. We have also experimented with the modification suggested by Tinker et al. (2012; see their Appendix A), which is identical to Eq. (66), except that they adopt  $r_\psi = r_{200}(M_1) + r_{200}(M_2)$  rather than Eq. (67). Not only do we find this method to be less accurate, especially for the lower mass bins, but the dependence of  $r_\psi$  on halo mass also makes the evaluation of  $Q(k|M_1, M_2, z)$  more CPU intensive.

Note though, that there is no guarantee that  $\psi = 0.9$  is also the best-fit parameter for any cosmology other than the one considered here. Hence, if we simply adopt  $\psi = 0.9$  when trying to constrain cosmological parameters, we might introduce an unwanted systematic bias. Fortunately, as we demonstrate in Paper II,  $\psi$  is only weakly degenerate with the cosmological parameters; most of its degeneracy is with the parameters that describe the satellite CLF. Hence, errors in  $\psi$  may result in systematic errors in the inferred satellite fractions, but will not significantly bias our constraints on

cosmological parameters. Nevertheless, in order to be conservative, we will marginalize over uncertainties in  $\psi$  when fitting for cosmological parameters (see Paper III).

### 4.3 Testing Halo Exclusion

Having calibrated the scale dependence of the halo bias, we now proceed to test the accuracy of our model in calculating  $\xi_{\text{gg}}$  and  $\xi_{\text{gm}}$ , focusing in particular on the accuracy of our treatment of halo exclusion. Using the mock galaxy distribution (hereafter MGD) of the L250 simulation box, we first compute the real-space correlation function for three different luminosity bins. The orange filled circles in the upper panels of Fig. 2 show the results thus obtained. In the panels in the middle row, we show the contribution to  $\xi_{\text{gg}}(r)$  from the 2-halo term (green filled circles), the 1-halo central-satellite term (purple filled circles) and the 1-halo satellite-satellite term (blue filled circles). In the high-luminosity bin (right-hand panels), the galaxy-galaxy correlation function is dominated by the 1-halo central-satellite term on small scales ( $r \lesssim 0.3h^{-1}$  Mpc), and by the 2-halo term on large scales ( $r \gtrsim 1.0h^{-1}$  Mpc). On intermediate scales, the 1-halo satellite-satellite term dominates. Note how this term becomes more and more dominant for less luminous galaxies; in fact in the lowest luminosity bin considered here (left-hand panels), the 1-halo satellite-satellite term completely dominates the signal for  $r \lesssim 1h^{-1}$  Mpc. This reflects the fact that the satellite fraction increases drastically from  $f_{\text{sat}} \simeq 0.136$  for the brightest bin, to  $f_{\text{sat}} \simeq 0.465$  for the intermediate luminosity bin, to  $f_{\text{sat}} \simeq 0.996$  for the faintest bin. Note, though, that these satellite fractions are unrealistic due to the adopted cut-offs in halo mass at  $M = 10^{12}h^{-1} M_\odot$  and  $10^{14.5}h^{-1} M_\odot$ . For example, for the CLF adopted here, virtually all central galaxies with  $r$ -band magnitudes (K-corrected to  $z = 0.1$ ) in the range  $-18 \geq^{0.1} M_r - 5 \log h \geq -19.5$  reside in haloes with  $M < 10^{12}h^{-1} M_\odot$ , which are not accounted for in our MGD; hence, almost all mock galaxies in this magnitude range are satellites. For comparison, if we were to integrate our CLF over the entire mass range from  $M = 0$  to  $M = \infty$ , the corresponding satellite fractions, given by

$$f_{\text{sat}}(L_1, L_2) = \frac{\int_{L_1}^{L_2} dL \int_0^\infty \Phi_s(L|M) n(M) dM}{\int_{L_1}^{L_2} \Phi(L) dL}, \quad (83)$$

are equal to  $f_{\text{sat}} = 0.334, 0.253,$  and  $0.167$  from the faintest to the brightest bin, respectively. Although the trends seen in Fig. 2 are stronger than what is expected in reality, we consider the fact that the dynamic range in  $f_{\text{sat}}$  covered is unrealistically large beneficial for the purpose of testing the accuracy of our model.

The solid lines in the panels in the upper and middle rows of Fig. 2 are the analytical results obtained using our fiducial model with halo exclusion and with  $\psi = 0.9$ . Here we have adopted the same cosmology, redshift and CLF parameters as for the MGD. Note that, once again, all integrals over halo mass are only integrated over the range  $10^{12}h^{-1} M_\odot \leq M \leq 10^{14.5}h^{-1} M_\odot$ , and we adopt  $k_{\text{min}} = \sqrt{3} \times (2\pi/L_{\text{box}})$  for the integration range in Eq. (42). Overall the agreement between our analytical prediction and the results from the MGD is extremely good. As is evident from the panels in the middle row, our treatment of halo ex-

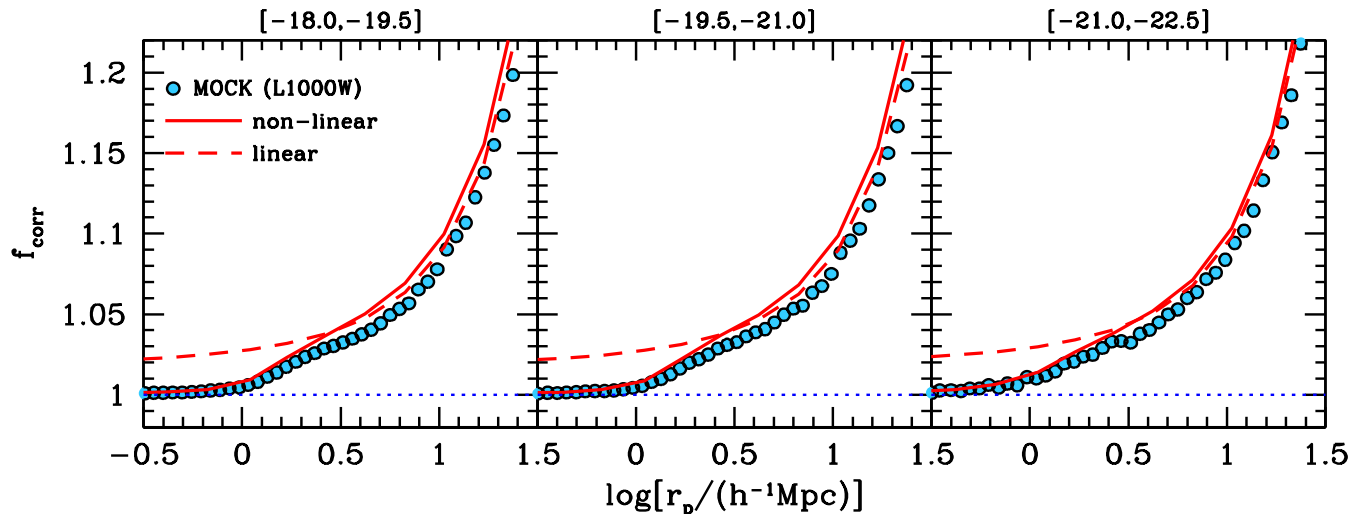


**Figure 5.** The correction factor,  $f_{\text{corr}}(r_p)$ , that describes the effect of residual redshift space distortions that arise from the use of a finite integration range when computing the projected correlation function, i.e., from Eq. (45) with a finite  $r_{\text{max}}$ . The shaded circles show the results obtained from the mock galaxy distribution in the L1000W simulation box with  $r_{\text{max}} = 40h^{-1}$  Mpc. Results are shown for the same three magnitude bins as in Figs. 2 - 4, as indicated. Dashed and solid curves correspond to the  $f_{\text{corr}}(r_p)$  obtained using the Kaiser formalism (see §2.3) with the linear and non-linear galaxy-galaxy correlation functions, respectively. The latter is in much better agreement with the mock results on small scales. See text for a detailed discussion.

clusion nicely captures the sudden decline of the 2-halo term on small scales. Although the analytical 2-halo term becomes less accurate for  $r \lesssim 0.5h^{-1}$  Mpc, mainly due to numerical issues, at these small scales the 1-halo term always dominates the total correlation function by at least an order of magnitude. Hence, this inaccuracy is of little practical concern. This is evident from the lower panels where we plot the difference between the model prediction and the true correlation function in the mock, normalized by the latter, as function of radius. Over the entire range  $0.01h^{-1}$  Mpc  $\leq r \lesssim 10h^{-1}$  Mpc the model predictions agree with the mock results to an accuracy of a few percent (typically  $< 5\%$ ). At the 1-halo to 2-halo transition scale ( $r \simeq 1h^{-1}$  Mpc), which has been notoriously difficult to model accurately, the errors are somewhat larger but always stay below 10%.

Fig. 3 shows the same as Fig. 2, but now for the galaxy-matter cross correlation,  $\xi_{\text{gm}}(r)$ . Similar trends are evident; the model's 2-halo term becomes less accurate on small scales, but this has little to no impact on the quality of the model as is evident from the lower panels. As for the galaxy-galaxy correlation function, the model agrees with the simulation results at the few percent level. In particular, it is noteworthy that the model is accurate at better than 10 percent on small scales. This indicates that non-sphericity of haloes, scatter in halo concentration, and halo substructure, all of which are ignored in our model, do not have a large ( $\gtrsim 10$  percent) impact on the results (see §5 for a detailed discussion).

#### 4.4 Testing the Approximate Linear Model

As we have demonstrated above, our implementation of halo exclusion and scale dependence of the bias are accurate at the few percent level. However, the required computation of  $Q(k|M_1, M_2, z)$ , defined in Eq. (20), is fairly CPU intensive. The computation of  $w_p(r_p)$  and  $\Delta\Sigma(R)$  for six luminosity

bins (i.e., a single model; see paper III) takes  $\sim 20$  seconds on a single (fast) processor. Consequently, the construction of an adequate Monte Carlo Markov Chain (which has to be large given that our model has anywhere from 14 to 19 free parameters, depending on the priors used) takes several days to complete (on a single processor). Although this is not a major challenge in light of the fact that most desktop computers nowadays have multiple processors, it nevertheless would be hugely advantageous if a much faster, approximate method could be found. In particular, the code can be made much faster if we were to ignore halo exclusion and/or the scale dependence of the halo bias.

In this section we therefore investigate the pros (increase in speed) and cons (decrease in accuracy) of two different simplifications of our model. The first simplification is to ignore halo exclusion, i.e., we set  $r_{\text{min}} = 0$  in Eq. (11). In that case we have that  $\xi_{\text{hh}}(r, z|M_1, M_2) = b_{\text{h}}(M_1, z)b_{\text{h}}(M_2, z)\zeta(r, z)\xi_{\text{mm}}(r, z)$ , and the two-halo term of the power spectrum (33) simplifies to

$$P_{\text{xy}}^{2\text{h}}(k, z) = \bar{b}_{\text{x}}(k, z)\bar{b}_{\text{y}}(k, z)P_{\text{ne}}(k, z), \quad (84)$$

where 'x' and 'y' are either 'c' (for central), 's' (for satellite), or 'm' (for matter),

$$\bar{b}_{\text{x}}(k, z) = \int dM \mathcal{H}_{\text{x}}(k, M, z) n(M, z) b_{\text{h}}(M, z), \quad (85)$$

with  $\mathcal{H}_{\text{x}}(k, M, z)$  given by Eqs. (34)–(36), and

$$P_{\text{ne}}(k, z) = 4\pi \int_0^\infty \zeta(r) \xi_{\text{mm}}(r, z) \frac{\sin kr}{kr} r^2 dr. \quad (86)$$

This simplified model has the great advantage that it does not require the tedious and CPU intensive evaluation of  $Q(k|M_1, M_2, z)$ , causing a speed-up of a factor  $\sim 10$ , while still accounting for the scale dependence of the halo bias. In what follows we shall refer to this model as the 'no-exclusion model'. The solid lines in Fig. 4 show the relative error in

$\xi_{\text{gg}}(r)$  of the no-exclusion model with respect to our fiducial model with halo exclusion. Results are shown for three magnitude bins, as indicated in the top panels, and for two different cosmologies/CLFs. In the upper panels we use the same cosmology and CLF as for the mocks described in §4.1. In the lower panels we use the WMAP3 cosmology, i.e., the cosmological parameters that best fit the three year data release of the Wilkinson Microwave Anisotropy Probe (Spergel et al. 2007) and the best-fit CLF model for that cosmology obtained by Cacciato et al. (2009). The main motivation for showing results for two different cases is to emphasize that the fractional errors of the no-exclusion model may vary quite significantly from one cosmology and/or CLF to another. Clearly the no-exclusion model in general overpredicts the galaxy-galaxy correlation functions on small scales ( $r \lesssim 2h^{-1}$  Mpc) by 20 to 50 percent<sup>¶</sup>.

At the risk of further deteriorating the accuracy of the model, we can make additional simplifications by replacing  $P_{\text{ne}}(k, z)$  in Eq. (84) by the linear matter power spectrum,  $P_{\text{mm}}^{\text{lin}}(k, z)$ . This results in the ‘linear’ halo model, which has been used previously by numerous authors (e.g., Ma & Fry 2000; Seljak 2000; Scoccimarro et al. 2001; Guzik & Seljak 2002; Mandelbaum et al. 2005; Seljak et al. 2005; see also Cooray & Sheth 2002 and Mo et al. 2010). This removes the need for the integration (86) and therefore further speeds up the computation, albeit at the cost of ignoring the scale dependence of the halo bias. The dashed curves in Fig. 4 show how these ‘linear’ galaxy-galaxy correlation functions compare to the fiducial model with halo exclusion and with scale dependence of halo bias. Somewhat surprisingly, for the cosmology+CLF shown in the upper panels, this linear model performs significantly better than the no-exclusion model, with errors that are always below 10 percent. This indicates that halo-exclusion and scale-dependence of halo bias have comparable but opposite effects on small scales ( $r \lesssim 1h^{-1}$  Mpc), which *may* roughly cancel each other. The lower panels, however, show that this is not always the case, and that the linear model can significantly underestimate the galaxy-galaxy correlation functions (by as much as 30-40 percent) in the 1-halo to 2-halo transition regime. In addition, the linear model typically overpredicts the correlation power on large scales of  $\sim 10h^{-1}$  Mpc by 10 percent. This is a well known effect that has already been discussed in numerous studies of the halo model (e.g., e.g., Ma & Fry 2000; Seljak 2000; Scoccimarro et al. 2001; Smith et al. 2003; Cole et al. 2005; Hayashi & White 2008). Finally we note that similar tests for the galaxy-matter cross correlation functions yield fractional errors for the no-exclusion and linear models that are very similar as for the galaxy-galaxy correlation functions shown in Fig. 4.

Hence, despite the order of magnitude increase in computational speed, we conclude that both the ‘no-exclusion’ model and the ‘linear’ model suffer from systematic inaccuracies that can easily reach 30 to 40 percent, which we consider inadequate for the purpose of constraining cosmological parameters. In Papers II and III we therefore exclusively use the much more accurate, but more CPU intensive,

model described in §2 above, which properly accounts for both halo exclusion and scale dependence of the halo bias.

#### 4.5 Redshift Space Distortions

As discussed in §2.3, the projected correlation functions used to constrain the models have been obtained using a finite range of integration along the line-of-sight. Consequently, they suffer from residual redshift space distortions (RRSDs) that need to be corrected for. In this section we investigate the magnitude of these RRSDs, as well as the accuracy of our correction method, which is based on the linear Kaiser formalism (Kaiser 1987). To that extent we use the mock galaxy distribution (MGD) obtained from the L1000W simulation box, as described in §4.1. We first use this MGD to compute the projected correlation function,  $w_{\text{p}}(r_{\text{p}})$ , for three luminosity bins, by integrating the corresponding  $\xi_{\text{gg}}(r_{\text{p}}, r_{\pi})$  out to  $r_{\text{max}} = 40h^{-1}$  Mpc<sup>||</sup>. Note that this is the same value of  $r_{\text{max}}$  as used by Zehavi et al. (2011) for computing the projected correlation functions of faint galaxies in the SDSS DR4. Next we compute the same  $w_{\text{p}}(r_{\text{p}})$ , but this time we set the peculiar velocities of all galaxies to zero, i.e., we simply set  $r_{\pi} = \sqrt{r^2 - r_{\text{p}}^2}$ , where  $r$  is the real-space separation between two galaxies. The ratio of these two ‘measurements’ of the projected correlation function, shown as filled circles in Fig. 5, indicates the error one makes in the estimate of  $w_{\text{p}}(r_{\text{p}})$  when ignoring the RRSDs, i.e., when computing  $w_{\text{p}}(r_{\text{p}})$  using

$$w_{\text{p}}(r_{\text{p}}) = 2 \int_{r_{\text{p}}}^{r_{\text{out}}} \xi_{\text{gg}}(r) \frac{r \, dr}{\sqrt{r^2 - r_{\text{p}}^2}}, \quad (87)$$

with  $r_{\text{out}} = \sqrt{r_{\text{p}}^2 + r_{\text{max}}^2}$ . As discussed in §2.3, this is the standard method used by numerous authors in the past. The MGD results in Fig. 5 show that ignoring RRSDs causes an error in  $w_{\text{p}}(r_{\text{p}})$  that exceeds 10 percent on scales  $\gtrsim 10h^{-1}$  Mpc. Note, though, that in the MGD we only populated haloes in the mass range  $10^{13}h^{-1} M_{\odot} \leq M \leq 10^{14.5}h^{-1} M_{\odot}$ . As we show below, using the full mass range results in RRSDs that are even larger.

The dashed line indicates the correction factor  $f_{\text{corr}}$  given by Eq. (48). This correction factor is based on the Kaiser formalism for the linear velocity field, and is computed using the *linear* galaxy-galaxy correlation function given by Eq. (49). Note that the resulting  $f_{\text{corr}}$  provides a fairly accurate description of the RRSDs resulting from using a finite  $r_{\text{max}}$ , at least at large scales. However, on small scales it clearly overpredicts  $f_{\text{corr}}$  by a few percent. Hence, using this correction factor would overpredict  $w_{\text{p}}(r_{\text{p}})$  by a similar amount on small scales.

The solid line shows the correction factor obtained by simply replacing  $\xi_{\text{gg}}^{\text{lin}}(r)$  in Eq. (48) and Eqs. (51)-(55) by the non-linear version  $\xi_{\text{gg}}(r)$ . Although the Kaiser formalism is strictly only valid in the linear regime, this simple modification works remarkably well; the model now accurately reproduces the mock results on small scales. On larger scales, the model somewhat overpredicts  $f_{\text{corr}}$  compared to the mock results. From the ratio between the two we estimate that

<sup>¶</sup> The sharp features apparent around  $0.3h^{-1}$  Mpc are not due to numerical noise, but are real manifestations of halo exclusion.

<sup>||</sup> Here we have assumed that the plane-parallel approximation holds



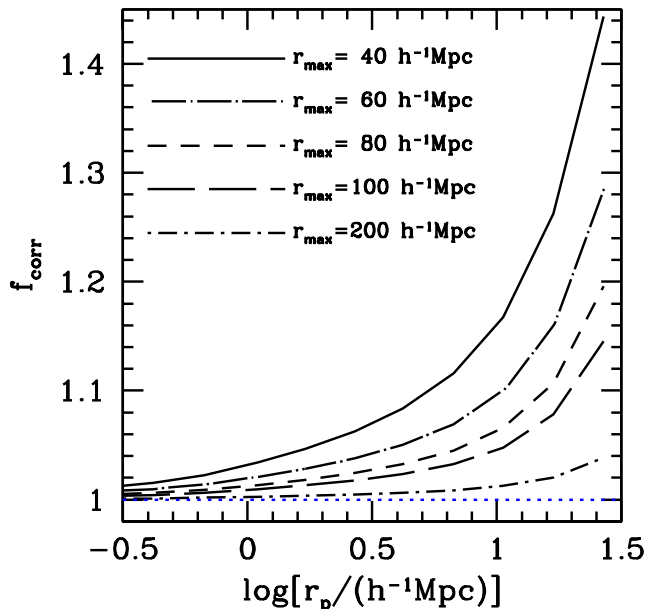


**Figure 6.** The RRSD correction factor,  $f_{\text{corr}}(r_p)$ , for different values of the integration range  $r_{\text{max}}$ , as indicated. All these correction factors have been obtained for galaxies with  $-21 \leq^{0.1} M_r - 5 \log h \leq -19.5$ , assuming the same cosmology and CLF as for the L1000W mock (i.e., similar to the middle column in Fig. 5). Note that  $f_{\text{corr}}$  for  $r_{\text{max}} = 40 h^{-1}$  Mpc is larger than in the case of Fig. 5; this is due to the fact that here we integrate over all halo masses, whereas in Fig. 5 we only considered haloes with  $10^{13} h^{-1} M_{\odot} \leq M \leq 10^{14.5} h^{-1} M_{\odot}$  in order to allow for a fair comparison with the mock results. Note also that even for  $r_{\text{max}} = 200 h^{-1}$  Mpc the correction factor exceeds 5 percent for  $r_p \gtrsim 30 h^{-1}$  Mpc.

the final error we make on  $w_p(r_p)$  from the imperfect correction for RRSDs is always less than 2 percent over the scales of interest.

Finally, having demonstrated that  $f_{\text{corr}}(r_p, z)$ , obtained using the non-linear galaxy-galaxy correlation function, provides an accurate description of the RRSDs that arise from using a finite integration range, we can use it to predict the magnitude of RRSDs for different values of  $r_{\text{max}}$ . Fig. 6 shows  $f_{\text{corr}}(r_p)$  for five different values of  $r_{\text{max}}$ , as indicated. Contrary to the results shown in Fig. 5, which only considered haloes in the mass range  $10^{13} h^{-1} M_{\odot} \leq M \leq 10^{14.5} h^{-1} M_{\odot}$  in order to allow for direct comparison with the mock results, the results in Fig. 6 have been obtained by integrating over all halo masses. Note that this results in  $f_{\text{corr}}$  values for  $r_{\text{max}} = 40 h^{-1}$  Mpc that are significantly larger than those in Fig. 5. In particular, using  $r_{\text{max}} = 40 h^{-1}$  Mpc without a correction for RRSDs, underestimates  $w_p(r_p)$  at  $r_p = 20 h^{-1}$  Mpc by  $\sim 35$  percent! Even when using  $r_{\text{max}} = 200 h^{-1}$  Mpc, the RRSDs causes errors in the projected correlation function that exceed 5 percent for  $r_p \gtrsim 30 h^{-1}$  Mpc. Clearly, correcting for RRSDs is extremely important, especially when using projected correlation functions to constrain cosmological parameters. The modified Kaiser method presented here corrects for these RRSDs to an accuracy of better than 2 percent.

## 5 SHAPES, ALIGNMENT, SUBSTRUCTURE AND CONTRACTION OF DARK HALOES

As discussed in §3.5, our model assumes that dark matter haloes are spheres with an NFW density profile. Clearly, this is a highly oversimplified picture. In reality, dark matter haloes are triaxial, have substructure, and have a density profile that may have been modified due to the action of galaxy formation. In addition, our model ignores the fact that there is significant scatter in the relation between halo mass and halo concentration. After discussing how each of these effect impacts the accuracy of our oversimplified model, we show how we can take these shortcomings into account by marginalizing over the normalization of the concentration-mass relation of dark matter haloes.

### 5.1 Halo Shapes and Alignment

The assumption that dark matter haloes are spherical is inconsistent with expectations based on numerical simulations (e.g., Jing & Suto 2002; Bailin & Steinmetz 2005; Allgood et al. 2006) and/or non-spherical collapse conditions (e.g., Zel'dovich 1970; Icke 1973; White & Silk 1979). As shown by Yang et al. (2004), assuming that haloes are spherical underestimates the correlation function obtained if haloes are represented by FOF groups in numerical simulations by as much as  $\sim 20$  percent on small scales ( $r \sim 0.1 h^{-1}$  Mpc). A similar test was recently performed by van Daalen, Angulo & White (2011), who basically came to the same conclusion. However, these tests of the impact of halo triaxiality are not directly applicable to our model. After all, our model uses halo mass functions and halo bias functions in which haloes are specifically *defined* as spherical volumes. Hence, a fair assessment of the impact of the non-spherical symmetry of dark matter haloes on our results should compare a correlation function in which it is assumed that all matter within the spherical volume of the halo has spherical symmetry (i.e., our model assumption) to one in which the dark matter particles and galaxies *within the same spherical volume* are given a more realistic distribution that is not spherically symmetric. Note that this is not the same as a comparison of spherical haloes to FOF haloes, since the latter typically do not occupy a spherical volume. As demonstrated by More et al. (2012, in preparation), this yields correlation functions that only differ at the 5 to 10 percent level. Detailed theoretical calculations by Smith & Watts (2005) reach a similar conclusion, that ignoring halo triaxiality only impacts the two-point correlation functions at the level of  $\sim 5$  percent. This is also consistent with Li et al. (2009), who performed detailed tests that showed that non-sphericity of dark matter haloes has only a small effect of  $\lesssim 5$  percent on the excess surface densities, and only on the smallest scales probed by the data. Hence, we conclude that our model assumption that haloes are spherical may underpredict both  $\xi_{\text{gg}}(r)$  and  $\xi_{\text{gm}}(r)$  on small scales ( $r < 1 h^{-1}$  Mpc), but by no more than  $\sim 10$  percent.

However, the fact that haloes have triaxial, rather than spherical shapes, also implies that another effect might in principle be important, namely halo alignment. Such potential alignment between haloes is not accounted for in our model, which therefore might cause systematic errors in our two-point correlation functions. However, Smith & Watts

(2005) have shown that a strict upper bound for the effect of intrinsic alignment is a 10 percent effect on the two-point correlation function (corresponding to a scenario with maximum alignment). Van Daalen et al. (2011) have shown that realistic amounts of alignment, as present in numerical simulations of structure formation in a  $\Lambda$ CDM cosmology, has an effect on the correlation functions that is not larger than  $\sim 2$  percent. We therefore conclude that potential halo alignment can be safely ignored.

## 5.2 Halo Concentrations

As discussed in §3.5, we assume that dark matter haloes have NFW density profiles with a concentration-mass relation given by Macciò et al. (2007), properly converted to our definition of halo mass. This ignores, however, that there is a substantial amount of scatter in the concentration-mass relation. In particular, numerical simulations show that the concentrations,  $c$ , for haloes of mass  $M$  at redshift  $z$  follow a log-normal distribution

$$P(c|M, z) dc = \frac{1}{\sqrt{2\pi} \sigma_{\text{inc}}} \exp\left[-\frac{(\ln c - \ln \bar{c})^2}{2\sigma_{\text{inc}}^2}\right] \frac{dc}{c}, \quad (88)$$

where  $\bar{c} = \bar{c}(M, z)$  is the median halo concentration for a halo of mass  $M$  at redshift  $z$ , and  $\sigma_{\text{inc}} \simeq 0.3$  (Jing 2000; Bullock et al. 2001; Wechsler et al. 2002; Sheth & Tormen 2004; Macciò et al. 2007). Because of this scatter, the proper  $\tilde{u}_h(k|M, z)$  to use in the halo model is

$$\tilde{u}_h(k|M, z) = \int \tilde{u}_h(k|M, z, c) p(c|M, z) dc \quad (89)$$

(Giocoli et al. 2010b). However, in order to speed up the computations, we ignore this scatter and simply use  $\tilde{u}_h(k|M, z) = \tilde{u}_h(k|\bar{c}(M, z))$  instead.

The impact of this oversimplification is shown in Fig. 7, where the symbols show  $\tilde{u}_h(k|M, z)/\tilde{u}_h(k|\bar{c}(M, z)) - 1$ , with  $\tilde{u}_h(k|M, z)$  given by Eq. (89). Results are shown for three different values of  $\sigma_{\text{inc}}$ , as indicated, and are obtained using  $M = 10^{12} h^{-1} M_\odot$  and  $\bar{c} = 10$ . Taking the scatter in halo concentration into account boosts  $\tilde{u}_h(k)$  on small scales ( $k \gtrsim 10 h \text{ Mpc}^{-1}$ ) by an amount that increases with  $\sigma_{\text{inc}}$  (see also Cooray & Hu 2001 and Giocoli et al. 2010b). For  $\sigma_{\text{inc}} = 0.3$  this boost is of the order of 10 percent. The solid lines in Fig. 7 show  $\tilde{u}_h(k|c)/\tilde{u}_h(k|\bar{c}) - 1$ , where  $c = \bar{c}(1 + 0.8\sigma_{\text{inc}}^2)$ . Although certainly not a perfect fit, this simple relation gives a reasonable description of the impact of ignoring the scatter in  $p(c|M, z)$ . It shows that for  $\sigma_{\text{inc}} = 0.3$ , the error made ignoring this scatter is similar to the error made if  $\bar{c}(M, z)$  is underestimated by a factor  $1 + 0.8\sigma_{\text{inc}}^2 \simeq 1.07$ . This is comparable to the differences in the  $\bar{c}(M, z)$  relation obtained by different authors (e.g., Eke, Navarro & Steinmetz 2001; Bullock et al. 2001; Macciò et al. 2007; Zhao et al. 2009). Hence, it is at least as important to obtain a more reliable calibration of the median of  $p(c|M, z)$  than to take account of its scatter. As we discuss in §5.5 below, because of these uncertainties, and because of other oversimplifications of our model, we will marginalize over the normalization of the concentration-mass relation,  $\bar{c}(M, z)$ , when constraining cosmological parameters (see Paper III). The results shown here indicate that such a marginalization also captures the inaccuracies arising from the fact that we ignore the scatter in  $p(c|M)$ .

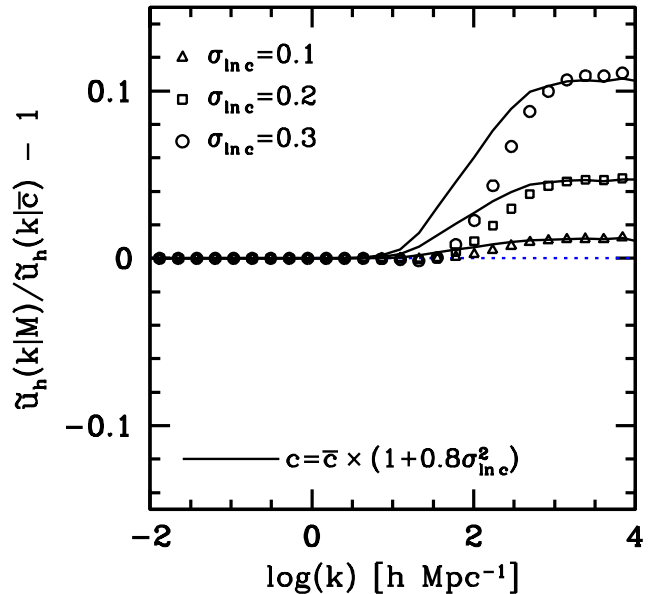


**Figure 7.** The ratio  $\tilde{u}_h(k|M)/\tilde{u}_h(k|\bar{c}) - 1$  as function of the wavenumber  $k$  for three different values of the scatter  $\sigma_{\text{inc}}$  in  $P(c|M)$ , as indicated (open symbols). Here  $\tilde{u}(k|M)$  is the Fourier Transform of the *average* normalized density profile of NFW haloes of mass  $M$ , properly accounting for the non-zero scatter in  $P(c|M)$  (Eq. [89]), while  $\tilde{u}_h(k|\bar{c})$  is the normalized density profile for the median halo concentration,  $\bar{c}$ . Hence, this ratio indicates the error made in  $\tilde{u}_h(k|M)$  when ignoring the scatter in halo concentration. The solid lines show the same ratio, but this time  $\tilde{u}(k|M)$  is computed under the assumption of zero scatter, and using a concentration parameter  $c = \bar{c}(1 + 0.8\sigma_{\text{inc}}^2)$ . The reasonable agreement with the open symbols indicates that, to good approximation, one can mimic the effect of non-zero scatter in  $P(c|M)$  by simply computing  $\tilde{u}(k|M)$  for a halo concentration that is a factor  $1 + 0.8\sigma_{\text{inc}}^2$  larger than the median concentration.

## 5.3 Halo Substructure

Another oversimplification of our model is that we assume that dark matter haloes have a smooth density distribution. However numerical simulations of hierarchical structure formation have shown that haloes are not smooth, but have a significant population of dark matter subhaloes (e.g., Moore et al. 1998; Springel et al. 2001). Approximately 10 percent of the mass of a dark matter halo is associated with these subclumps, with a weak dependence on halo mass and cosmology (e.g., Gao et al. 2004; van den Bosch et al. 2005b; Giocoli et al. 2008, 2010a). Since these subhaloes are believed to host satellite galaxies, they will impact the galaxy-matter cross correlation function on small scales. Although formalisms to include dark matter substructure in the halo model have been developed (e.g., Sheth & Jain 2003; Giocoli et al. 2010b), the implementation is numerically cumbersome in that it adds a number of integrations, causing a very significant increase in the computation time per model. In addition, the model still involves a number of uncertainties, such as the density profiles of dark matter subhaloes.

Fortunately, as shown by Mandelbaum et al. (2005), Yoo et al. (2006) and Li et al. (2009), the impact of substructure is negligible on the radial scales of interest, i.e., on the scales for which we currently have data on  $\Delta\Sigma(R)$  available ( $R \gtrsim 0.05 h^{-1} \text{ Mpc}$ ). Hence, we conclude that we

do not make significant errors by ignoring dark matter substructure.

#### 5.4 The Impact of Baryons

Although numerical simulations of structure formation have established that dark matter haloes follow a universal profile that is accurately described by the NFW profile (Eq. [68]), this ignores the impact of baryons. During the process of galaxy formation, baryons collect at the center of the halo potential well and may subsequently be expelled due to feedback processes. Because of the gravitational interaction between baryons and dark matter, the dark matter halo will respond to this galaxy formation process.

It is often assumed that the impact of baryons is to cause (adiabatic) contraction of the dark matter haloes (e.g., Blumenthal et al. 1986; Gnedin et al. 2004; Abadi et al. 2010; see also Schulz, Mandelbaum & Padmanabhan 2010; More et al. 2012b for observational support). However, it is also possible for haloes to expand in response to galaxy formation; rapid mass-loss from the galaxy due to (repetitive) feedback from supernovae and/or AGN (e.g., Pontzen & Governato 2012), dynamical friction operating on baryonic clumps (e.g., El-Zant, Shlosman & Hoffman 2001; Mo & Mao 2004), and galactic bars (e.g., Weinberg & Katz 2002) all may cause dark matter haloes to become less centrally concentrated than their ‘pristine’ (i.e., without galaxy formation) counterparts.

Interestingly, both galaxy rotation curves and galaxy scaling relations suggest that dark matter haloes are less centrally concentrated than what is expected in the absence of baryonic processes in a CDM dominated universe (e.g., Swaters et al. 2003; de Blok et al. 2008; Dutton et al. 2007, 2011; Trujillo-Gomez et al. 2011). Although this may suggest that galaxy formation indeed results in a net halo expansion, it may also indicate that dark matter is not dark, but warm (e.g., Sommer-Larsen & Dolgov 2000) or self-interacting (e.g., Spergel & Steinhardt 2000).

We conclude that the detailed density profiles of dark matter haloes carry a significant uncertainty, which needs to be accounted for.

#### 5.5 Marginalization

All the effects discussed above, regarding halo shape, scatter in halo concentrations, halo substructure, and halo contraction/expansion, impact the 1-halo terms of the correlation functions by either boosting or suppressing power on small scales. What is ultimately of importance for the accuracy of our models is the *combined* impact of all these effects.

The combined impact of all effects except for that of halo contraction/expansion can be gauged from the lower panels of Fig. 3, which show that our model is consistent with the simulation results, in which the haloes have realistic, triaxial density distributions, have substructure, and have non-zero scatter in the concentration-mass relation, to better than 10 percent. This test therefore confirms that our oversimplifications are accurate at the 10 percent level.

We caution, though, that this test does not account for possible halo contraction/expansion due to baryons, whose impact is difficult to gauge in the absence of a more detailed

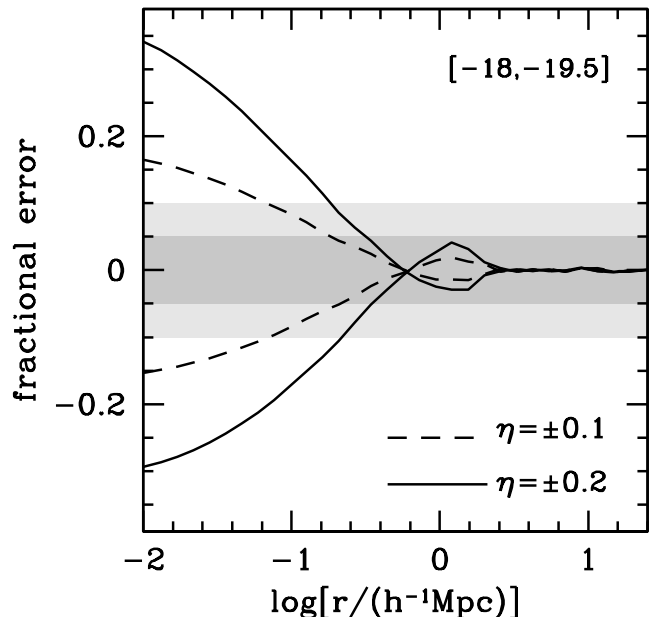


**Figure 8.** The impact on the galaxy-matter cross correlation function,  $\xi_{\text{gm}}(r)$  of multiplying the normalization of the concentration-mass relation,  $c(M)$ , of dark matter haloes by a factor  $(1 + \eta)$ , where  $\eta = \pm 0.1$  (dashed lines) or  $\eta = \pm 0.2$  (solid lines). Here we have, once again, adopted the same cosmology and CLF as for the mocks described in §4.1.

understanding of galaxy formation. Hence, when constraining cosmological parameters (see Paper III), we will take all these oversimplifications regarding the density distributions of dark matter haloes into account by marginalizing over the normalization of the concentration-mass relation,  $\bar{c}(M, z)$ . In particular, we introduce the parameter  $\eta$ , so that the concentration for a halo of mass  $M$  is given by  $(1 + \eta) \times \bar{c}(M, z)$ , where  $\bar{c}(M, z)$  is the average concentration-mass relation of Macciò et al. (2007), properly converted to our definition of halo mass. As a prior we assume that the probability distribution function (PDF) for  $\eta$  is given by

$$P(\eta) = \frac{1}{\sqrt{2\pi}\sigma_\eta} \exp\left(-\frac{\eta^2}{2\sigma_\eta^2}\right) \quad (90)$$

where we adopt  $\sigma_\eta = 0.1$ . Fig. 8 shows the impact of  $\eta$  on the galaxy-matter cross-correlation function for galaxies with magnitudes in the range  $-18 \geq {}^{0.1}M_r - 5 \log h \geq -19.5$  (results for other magnitude bins are very similar). The dashed and solid lines show the fractional changes in  $\xi_{\text{gm}}(r)$  for  $\eta = \pm 0.1$  and  $\pm 0.2$ , respectively, which correspond to the 68 and 95 percent confidence intervals of the prior PDF. Note how  $\eta = \pm 0.2$  modifies the one-halo term of  $\xi_{\text{gm}}(r)$  by more than 20 percent on small scales ( $r < 0.1 h^{-1}$  Mpc), which we argue is more than adequate to capture the inaccuracies in our model that arise from the various oversimplifications discussed above (see Paper III for more details, and for a discussion of the posterior distribution of  $\eta$  and its implications).

## 6 CONCLUSIONS

Galaxies are abundant and visible to high redshifts, making them, in principle, excellent tracers of the mass distribution in the Universe over cosmological scales. The problem, however, is that galaxies are biased tracers, and that this bias is a complicated function of scale, luminosity, morphological type, etc. It is an imprint of the poorly understood physics related to galaxy formation. On sufficiently large scales, galaxy bias is expected to be scale-independent with a value that is known to depend on a variety of galaxy properties such as luminosity and color (e.g., Norberg et al. 2001, 2002; Zehavi et al. 2005, 2011; Wang et al. 2007). On small, (quasi) non-linear scales ( $r \lesssim 3h^{-1}$  Mpc), galaxy bias becomes strongly scale-dependent (e.g., Cacciato et al. 2012a), making it extremely difficult to infer any constraints on cosmology, without having a proper, detailed method of either measuring this bias or marginalizing over it. For this reason, almost all studies to date that used the distribution of galaxies in order to constrain cosmological parameters have focused on large, linear scales, and treated galaxy bias as a ‘nuisance parameter’ that needs to be marginalized over.

In this paper, the first in a series, we have presented a new method, similar to that of Yoo et al. (2006) and Leauthaud et al. (2011), that can simultaneously solve for cosmology and galaxy bias on small, non-linear scales. The method uses the halo model to analytically describe the (non-linear) matter distribution, and the conditional luminosity function (CLF) to specify the halo occupation statistics. For a given choice of cosmological parameters, which determine the halo mass function, the halo bias function, and the (non-linear) matter power spectrum, this model can be used to predict the galaxy luminosity function, the two-point correlation functions of galaxies as function of both scale and luminosity, and the galaxy-galaxy lensing signal, again as function of both scale and luminosity. These are all observables that have been measured at unprecedented accuracies from the Sloan Digital Sky Survey, and can therefore be used to constrain cosmological parameters.

In this paper we presented, in detail, our analytical framework, which is characterized by

- a treatment for scale dependence of halo bias on small scales, using a modified version of the empirical fitting function of Tinker et al. (2005).
- a proper treatment for halo exclusion, similar to that of Smith et al. (2007), which is correct under the assumption that dark matter haloes are spherical.
- a correction for residual redshift space distortions (RRSDs) using a slightly modified version of the linear Kaiser formalism.

We have tested the accuracy of our analytical model using detailed mock galaxy distributions, constructed using high-resolution numerical  $N$ -body simulations. We have shown that our analytical model is accurate to better than 10 percent (in most cases better than 5 percent), in reproducing the 3-dimensional galaxy-galaxy correlation and the galaxy matter correlation in the mock galaxy distributions over a wide range of scales ( $0.03h^{-1}$  Mpc  $\lesssim r \lesssim 30h^{-1}$  Mpc). In order to reach this level of accuracy we had to introduce, and tune, one free parameter that describes a modification of the empirical fitting function of Tinker et al. (2005) for the radial

halo bias dependence. This modification is required because this fitting function is only valid for a particular definition of halo mass that is different than the one adopted here (see also Tinker et al. 2012). When fitting the data in order to constrain cosmological constraints, we will marginalize over uncertainties in this free parameter (see Papers II and III). We have demonstrated that ignoring halo exclusion and/or the scale dependence of the halo bias results in errors in  $\xi_{gg}(r)$  and  $\xi_{gm}(r)$  in the 1-halo to 2-halo transition regime ( $r \sim 1h^{-1}$  Mpc) that can easily be as large as 40 percent. The correction for RRSDs is necessary because projected correlation functions are always obtained by integrating along the line-of-sight out to a finite radius (typically  $r_{\max} \sim 40 - 80h^{-1}$  Mpc) rather than out to infinity. In agreement with the results of Norberg et al. (2009), we show that not taking these RRSDs into account results in systematic errors that can easily exceed 20 percent on large scales ( $r_p \gtrsim 10h^{-1}$  Mpc), which can cause systematic errors in the inferred galaxy bias (see More 2011). As we demonstrate in Paper III, when unaccounted for these RRSDs can also result in significant systematic errors in the inferred cosmological parameters. Fortunately, as we have demonstrated, it is fairly straightforward to correct for these RRSDs, to an accuracy better than  $\sim 2$  percent, using a mildly modified version of the linear Kaiser formalism (Kaiser 1987).

Finally, the good accuracy of our analytical model on small scales for the galaxy-matter and halo-matter cross correlation functions (better than 10 percent) indicates that ignoring halo triaxiality, halo substructure, and scatter in the halo concentration-mass relation does not have a large impact, contrary to recent claims by van Daalen et al. (2011) who argue that halo triaxiality alone may cause inaccuracies as large as 20 percent. We argue that this apparent discrepancy mainly owes to different definitions of dark matter haloes (see discussion in § 5.1). Nevertheless, we have shown that, in order to be conservative, one can take these inaccuracies that arise from oversimplifications of the halo mass distributions into account by marginalizing over uncertainties in the normalization of the concentration-mass relation of dark matter haloes.

As indicated above, this is the first paper in a series. In Paper II (More et al. 2012a), we perform a Fisher matrix analysis to (i) investigate the strength of each of the datasets (luminosity function, projected correlation functions, and excess surface densities), (ii) identify various degeneracies between our model parameters, and (iii) forecast the accuracy with which various cosmological parameters and CLF parameters can be constrained with current data. In Paper III (Cacciato et al. 2012b) we apply our method to data from the Sloan Digital Sky Survey and present the resulting constraints on both cosmological parameters (fully marginalized over the uncertainties related to galaxy bias) and the CLF parameters (fully marginalized over uncertainties in cosmological parameters).

## ACKNOWLEDGMENTS

The work presented in this paper has greatly benefited from discussions with Matthew Becker, Alexie Leauthaud, Nikhil Padmanabhan, Eduardo Rozo, Roman Scoccimarro, Jeremy Tinker, Risa Wechsler, Idit Zehavi and Zheng Zheng. The

analysis of numerical simulations used in this work has been performed on the Joint Fermilab - KICP Supercomputing Cluster, supported by grants from Fermilab, Kavli Institute for Cosmological Physics, and the University of Chicago. FvdB acknowledges support from the Lady Davis Foundation for a Visiting Professorship at Hebrew University. This research was supported in part by the National Science Foundation under Grant No. NSF PHY11-25915 and NSF PHY-0551142.

## REFERENCES

- Abadi M.G., Navarro J.F., Fardal M., Babul A., Steinmetz M., 2010, *MNRAS*, 407, 435
- Abazajian K., et al., 2005, *ApJ*, 625, 613
- Adelman-McCarthy J.K., et al., 2006, *ApJS*, 162, 38
- Allgood B., Flores R.A., Primack J.R., Kravtsov A.V., Wechsler R.H., Faltenbacher A., Bullock J.S., 2006, *MNRAS*, 367, 1781
- Anderson, L., Aubourg, E., Bailey, S., et al. 2012, *arXiv:1203.6594*
- Bailin J., Steinmetz M., 2005, *ApJ*, 627, 647
- Baldauf T., Smith R.E., Seljak U., Mandelbaum R., 2010, *Phys. Rev. D.*, 81, 063531
- Beers T.C., Tonry J.L., 1986, *ApJ*, 300, 557
- Bennett C.L., et al., 2003, *ApJ*, 583, 1
- Berlind A.A., Weinberg D.H., 2002, *ApJ*, 575, 587
- Berlind A.A., et al., 2003, *ApJ*, 593, 1
- Blake C., et al., 2011, *MNRAS*, 415, 2892
- Blanton M.R. et al., 2003, *ApJ*, 592, 819
- Blumenthal G.R., Faber S.M., Flores R., Primack J.R., 1986, *ApJ*, 301, 27
- Boylan-Kolchin M., Springel V., White S.D.M., Jenkins A., 2010, *MNRAS*, 406, 896
- Brainerd T.G., Blandford R.D., Smail I., 1996, *ApJ*, 466, 623
- Bullock J.S., Kolatt T.S., Sigad Y., Somerville R.S., Kravtsov A.V., Klypin A.A., Primack J.R., Dekel A., 2001, *MNRAS*, 321, 559
- Bullock J.S., Wechsler R.H., Somerville R.S., 2002, *MNRAS*, 329, 246
- Busha M.T., Wechsler R.H., Behroozi P.S., Gerke B.F., Klypin A.A., Primack J.R., 2011, *ApJ*, 743, 11
- Cacciato M., van den Bosch F.C., More S., Li R., Mo H.J., Yang X., 2009, *MNRAS*, 394, 929
- Cacciato M., Lahav O., van den Bosch F.C., Hoekstra H., Dekel A., 2012a, preprint (*arXiv:1203.2616*)
- Cacciato M., van den Bosch F.C., More S., Mo H.J., Yang X., 2012b, submitted (paper III)
- Carlberg R.G., Yee H.K.C., Ellingson E., 1997, *ApJ*, 478, 462
- Chen J., 2008, *A&A*, 384, 347
- Cole S., et al., 2005, *MNRAS*, 362, 505
- Colless M., et al., 2003, preprint (*arXiv:astro-ph/0306581*)
- Collister A.A., Lahav O., 2005, *MNRAS*, 361, 415
- Cooray A., Hu W., 2001, *ApJ*, 554, 56
- Cooray A., Sheth R.K., 2002, *Phys. Rep.*, 372, 1
- Cooray A., Milosavljevic M., 2005, *ApJ*, 627, L89
- Crocce M., Scoccimarro R., 2006, *Phys. Review D*, 73, 063519
- Crocce M., Scoccimarro R., 2008, *Phys. Review D*, 77, 023533
- Davis M., Peebles P.J.E., 1983, *ApJ*, 267, 465
- Davis M., Efstathiou G., Frenk C.S., White S.D.M., 1985, *ApJ*, 292, 371
- de Blok W.J.G., Walter F., Brinks E., Trachternach C., Oh S.-H., Kennicutt R.C., 2008, *AJ*, 136, 2648
- Dunkley J., et al., 2009, *ApJS*, 180, 306
- Dutton A.A., van den Bosch F.C., Dekel A., Courteau S., 2007, *ApJ*, 654, 27
- Dutton A.A., et al., 2011, *MNRAS*, 416, 322
- Eisenstein D.J., Hu W., 1998, *ApJ*, 496, 605
- Eisenstein D.J., et al., 2005, *ApJ*, 633, 560
- Eke V.R., Navarro J.F., Steinmetz M., 2001, *ApJ*, 554, 114
- Elia A., Kulkarni S., Porciani C., Pietroni M., Matarrese S., 2011, *MNRAS*, 416, 1703
- El-Zant A.A., Shlosman I., Hoffman Y., 2001, *ApJ*, 560, 636
- Fisher P., et al., 2000, *AJ*, 120, 1198
- Fry J.N., Gaztanaga E., 1993, *ApJ*, 413, 447
- Gao L., White S.D.M., Jenkins A., Stoehr F., Springel V., 2004, *MNRAS*, 355, 819
- Gaztanaga E., Cabré A., Hui L., 2009, *MNRAS*, 399, 1663
- Gnedin O.Y., Kravtsov A.V., Klypin A.A., Nagai D., 2004, *ApJ*, 616, 16
- Giocoli C., Tormen G., van den Bosch F.C., 2008, *MNRAS*, 386, 2135
- Giocoli C., Tormen G., Sheth R.K., van den Bosch F.C., 2010a, *MNRAS*, 404, 502
- Giocoli C., Bartelmann M., Sheth R.K., Cacciato M., 2010b, *MNRAS*, 408, 300
- Guzik J., Seljak U., 2001, *MNRAS*, 321, 439
- Guzik J., Seljak U., 2002, *MNRAS*, 325, 311
- Hamilton A.J.S., 1992, *ApJ*, 385, L5
- Hayashi E., White S.D.M., 2008, *MNRAS*, 388, 2
- Hoekstra H., van Waerbeke L., Gladders M.D., Mellier Y., Yee H.K.C., 2002, *ApJ*, 577, 604
- Hütsi G., 2006, *A&A*, 449, 891
- Icke V., 1973, *A&A*, 27, 1
- Jing Y.P., 2000, *ApJ*, 535, 30
- Jing Y.P., Mo H.J., Börner G., 1998, *ApJ*, 503, 37
- Jing Y.P., Suto Y., 2002, *ApJ*, 574, 538
- Jing Y.P., Börner G., Suto Y., 2002, *ApJ*, 564, 15
- Kaiser N., 1987, *MNRAS*, 227, 1
- Komatsu E., et al., 2009, *ApJS*, 180, 330
- Komatsu E., et al., 2011, *ApJS*, 192, 18
- Kravtsov A.V., Klypin A.A., Khokhlov A.M., 1997, *ApJS*, 111, 73
- Kravtsov A.V., Berlind A.A., Wechsler R.H., Klypin A.A., Gottlöber S., Allgood B., Primack J.R., 2004, *ApJ*, 609, 35
- Leauthaud A., et al., 2007, *ApJS*, 172, 219
- Leauthaud A., Tinker J., Behroozi P.S., Busha M.T. Wechsler, R.H., 2011, *ApJ*, 738, 45
- Leauthaud A., et al., 2012, *ApJ*, 744, 159
- Lee K.-S., Giavalisco, M., Gnedin O.Y., Somerville R., Ferguson H., Dickinson M., Ouchi M., 2006, *ApJ*, 642, 63
- Li R., Mo H.J., Zuhui F., Cacciato M., van den Bosch F.C., Yang X., More S., 2009, *MNRAS*, 394, 1016
- Lin Y.-T., Mohr J.J., Stanford S.A., 2004, *ApJ*, 610, 745
- Ma C.-P., Fry J.N., 2000, *ApJ*, 543, 503
- Macciò A.V., Dutton A.A., van den Bosch F.C., Moore B., Potter D., Stadel J., 2007, *MNRAS*, 378, 55
- Magliocchetti M., Porciani C., 2003, *MNRAS*, 346, 186
- Mandelbaum R., Tasitsiomi A., Seljak U., Kravtsov A.V., Wechsler R.H., 2005, *MNRAS*, 362, 1451
- Mandelbaum R., Seljak U., Kauffmann G., Hirata C.M., Brinkmann J., 2006, *MNRAS*, 368, 715
- Mandelbaum R., Li C., Kauffmann G., White S.D.M., 2009, *MNRAS*, 393, 377
- Masjedi M., et al., 2006, *ApJ*, 644, 54
- Mather J.C., Fixsen D.J., Shafer R.A., Mosier C., Wilkinson D.T., 1999, *ApJ*, 512, 511
- McDonald P., 2006, *Phys. Rev. D.*, 74, 103512
- McDonald P., 2007, *Phys. Rev. D.*, 74, 043514
- Miralda-Escudé J., 1991, *ApJ*, 370, 1
- Mo H.J., Mao S., 2004, *MNRAS*, 353, 829
- Mo H.J., White S.D.M., 1996, *MNRAS*, 282, 347
- Mo H.J., Jing Y.P., White S.D.M., 1997, *MNRAS*, 284, 189
- Mo H.J., van den Bosch F.C., White S.D.M., 2010, *Galaxy Formation and Evolution*, Cambridge University Press, Cambridge

- Moore B., Governato F., Quinn T., Stadel J., Lake G., 1998, *ApJ*, 499, L5
- More S. van den Bosch F.C., Cacciato M., Mo H.J., Yang X., Li R., 2009a, *MNRAS*, 392, 801
- More S. van den Bosch F.C., Cacciato M., 2009b, *MNRAS*, 392, 917
- More S., van den Bosch F.C., Cacciato M., Skibba R., Mo H.J., Yang X., 2011, *MNRAS*, 410, 210
- More S., 2011, *ApJ*, 741, 19
- More S. van den Bosch F.C., Cacciato M., More A., Mo H.J., Yang X., 2012a, submitted (paper II)
- More A., Cabanac R., More S., Alard C., Limousin M., Kneib J.-P., Gavazzi R., Motta V., 2012b, *ApJ*, 749, 38
- Navarro J.F., Frenk C.S., White S.D.M., 1997, *ApJ*, 490, 493
- Neyman J., Scott E.L., 1952, *ApJ*, 116, 144
- Norberg P., et al., 2001, *MNRAS*, 328, 64
- Norberg P., et al., 2002, *MNRAS*, 332, 827
- Norberg P., Baugh C.M., Gaztanaga E., Croton D.J., 2009, *MNRAS*, 396, 19
- Padmanabhan N., White M., Eisenstein D.J., 2007, *MNRAS*, 376, 1702
- Padmanabhan N., et al., 2007, *MNRAS*, 378, 852
- Peacock J.A., Smith R.E., 2000, *MNRAS*, 318, 1144
- Percival W.J., et al., 2001, *MNRAS*, 327, 1297
- Percival W.J., et al., 2007a, *ApJ*, 657, 51
- Percival W.J., et al., 2007b, *ApJ*, 657, 645
- Percival W.J., et al., 2007c, *MNRAS*, 381, 1054
- Percival W.J., et al., 2010, *MNRAS*, 401, 2148
- Pontzen A., Governato F., 2012, *MNRAS*, 421, 3464
- Porciani C., Magliocchetti M., Norberg P., 2004, *MNRAS*, 355, 1010
- Saunders W., et al., 2000, *MNRAS*, 317, 55
- Schulz A. E., Mandelbaum R., Padmanabhan N., 2010, *MNRAS*, 408, 1463
- Scoccimarro R., Sheth R.K., Hui L., Jain B., 2001, *ApJ*, 546, 20
- Seljak U., 2000, *MNRAS*, 318, 203
- Seljak U., et al., 2005, *Phys. Rev. D*, 71, 043511
- Shectman S.A., et al., 1996, *ApJ*, 470, 172
- Sheldon E.S., et al., 2004, *AJ*, 127, 2544
- Sheldon E.S., et al., 2009, *ApJ*, 703, 2217
- Sheth R.K., Jain B., 2003, *MNRAS*, 345, 529
- Sheth R.K., Tormen G., 2004, *MNRAS*, 350, 1385
- Smith R.E., et al., 2003, *MNRAS*, 341, 1311
- Smith R.E., Scoccimarro R., Sheth R.K., 2007, *Phys. Rev. D.*, 75, 063512
- Smith R.E., Watts P.I.R., 2005, *MNRAS*, 360, 203
- Smith R.E., Desjacques V., Marian L., 2011, *Phys. Rev. D.*, 83, 043526
- Sommer-Larsen J., Dolgov A., 2001, *ApJ*, 551, 608
- Spergel D.N., Steinhardt P.J., 2000, *Phys. Rev. Lett.*, 83, 3760
- Spergel D.N., et al., 2003, *ApJS*, 148, 175
- Spergel D.N., et al., 2007, *ApJS*, 170, 377
- Springel V., White S.D.M., Tormen G., Kauffmann G., 2001, *MNRAS*, 328, 726
- Swaters R.A., Madore B.F., van den Bosch F.C., Balcells M., 2003, *ApJ*, 583, 732
- Takada M., Jain B., 2003, *MNRAS*, 340, 580
- Tal T., Wake D.A., van Dokkum P.G., 2012, *ApJ*, 751, 5
- Tegmark M., et al., 2006, *Phys. Rev. D.*, 74, 123507
- Tinker J.L., 2007, *MNRAS*, 374, 477
- Tinker J.L., Weinberg D.H., Zheng Z., Zehavi I., 2005, *ApJ*, 631, 41
- Tinker J.L., Weinberg D.H., Zheng Z., 2006, *MNRAS*, 368, 85
- Tinker J.L., Weinberg D.H., Warren M.S., 2006, *ApJ*, 647, 737
- Tinker J.L., Norberg P., Weinberg D.H., Warren M.S., 2007, *ApJ*, 659, 877
- Tinker J.L., Kravtsov A.V., Klypin A., Abazajian K., Warren M., Yepes G., Gottlöber S., Holz D.E., 2008, *ApJ*, 688, 709
- Tinker J.L., Robertson B.E., Kravtsov A.V., Klypin A., Warren M., Yepes G., Gottlöber S., 2010, *ApJ*, 724, 878
- Tinker J.L., et al., 2012, *ApJ*, 745, 16
- Trujillo-Gomez S., Klypin A., Primack J., Romanowsky A. J., 2011, *ApJ*, 472, 16
- van Daalen M.P., Angulo R.E., White S.D.M., 2011, preprint (arXiv:1110.4888)
- van den Bosch F.C., Yang X., Mo H.J., 2003a, *MNRAS*, 340, 771
- van den Bosch F.C., Mo H.J., Yang X., 2003b, *MNRAS*, 345, 923
- van den Bosch F.C., Norberg P., Mo H.J., Yang X., 2004, *MNRAS*, 352, 1302
- van den Bosch F.C., Yang X., Mo H.J., Norberg P., 2005a, *MNRAS*, 356, 1233
- van den Bosch F.C., Tormen G., Giocoli C., 2005b, *MNRAS*, 359, 1029
- van den Bosch F.C., et al., 2007, *MNRAS*, 376, 841
- van der Marel R.P., Magorrian J., Carlberg R.G., Yee H.K.C., Ellingson E., 2000, *AJ*, 119, 2038
- van Uitert E., Hoekstra H., Velander M., Gilbank D.G., Gladders M.D., Yee H.K.C., 2011, *A&A*, 534, 14
- Wake D.A., et al., 2008a, *MNRAS*, 387, 1054
- Wake D.A., Croom S.M., Sadler E.M., Johnston H.M., 2008b, *MNRAS*, 391, 1674
- Wang Y., Yang X., Mo H.J., van den Bosch F.C., Chu Y., 2004, *MNRAS*, 353, 287
- Wang Y., Yang X., Mo H.J., van den Bosch F.C., 2007, *ApJ*, 664, 608
- Watson D.F., Berlind A.A., McBride C.K., Masjedi M., 2010, *ApJ*, 709, 115
- Watson D.F., Berlind A.A., McBride C.K., Hogg D.W., Jiang T., 2012, *ApJ*, 749, 83
- Wechsler R.H., Bullock J.S., Primack J.R., Kravtsov A.V., Dekel A., 2002, *ApJ*, 568, 52
- Weinberg M.D., Katz N., 2002, *ApJ*, 580, 627
- White S.D.M., Silk J., 1979, *ApJ*, 231, 1
- Yang X., Mo H.J., van den Bosch F.C., 2003, *MNRAS*, 339, 1057
- Yang X., Mo H.J., Jing Y.P., van den Bosch F.C., Chu Y., 2004, *MNRAS*, 350, 1153
- Yang X., Mo H.J., van den Bosch F.C., Weinmann S.M., Li C., Jing Y.P., 2005, *MNRAS*, 362, 711
- Yang X., Mo H.J., van den Bosch F.C., Pasquali A., Li C., Barden M., 2007, *ApJ*, 671, 153 (Y07)
- Yang X., Mo H.J., van den Bosch F.C., 2008, *ApJ*, 676, 248
- Yoo J., Tinker J.L., Weinberg D.H., Zheng Z., Katz N., Davé R., 2006, *ApJ*, 652, 26
- Yoo J., Weinberg D.H., Tinker J.L., Zheng Z., Warren M.S., 2009, *ApJ*, 698, 967
- York D.G., et al., 2000, *AJ*, 120, 1579
- Zehavi I., et al. 2004, *ApJ*, 608, 16
- Zehavi I., et al., 2005, *ApJ*, 630, 1
- Zehavi I., et al., 2011, *ApJ*, 736, 59
- Zel'dovich Ya.B., 1970, *A&A*, 5, 84
- Zhao D.H., Jing Y.P., Mo H.J., Börner G., 2009, *ApJ*, 707, 354
- Zheng Z., 2004, *ApJ*, 610, 61
- Zheng Z., Tinker J.L., Weinberg D.H., Berlind A.A., 2002, *ApJ*, 575, 617
- Zheng Z., Coil A., Zehavi I., 2007, *ApJ*, 667, 760
- Zheng Z., Zehavi I., Eisenstein D.J., Weinberg D.H., Jing Y.P., 2009, *ApJ*, 707, 554